IDEA League

Structural wave propagation in unconsolidated granulates

Louis James Evans

August 10, 2018

Structural wave propagation in unconsolidated granulates

MASTER OF SCIENCE THESIS

for the degree of Master of Science in Applied Geophysics at
ETH Zürich

by

Louis James Evans

August 10, 2018

Department of Earth Sciences · ETH Zürich

ETH

Eidgenössische Technische Hochschule Zürich
Swiss Federal Institute of Technology Zurich

IDEA LEAGUE
JOINT MASTER'S IN APPLIED GEOPHYSICS

Delft University of Technology, The Netherlands
ETH Zürich, Switzerland
RWTH Aachen, Germany

Dated: *August 10, 2018*

Committee Members:

—————————————————————
Dr. Cornelis Weemstra

Supervisor(s):   Dr. Bart Van Damme

Dr. Dirk-Jan van Manen

Abstract

Unconsolidated granulates exhibit complex, nonlinear behaviour when subjected to dynamic forces. The presence of granular contacts gives this type of material a relatively low stiffness and provides hysteretic energy losses. These features make unconsolidated granulates suitable for railway ballast as it provides dissipation of vibrational energy from passing trains which is important to minimise vibrational disturbance. However, simulating the response of the railway superstructure under dynamic loads becomes difficult due to the nonlinearity of the ballast. In order to develop better prediction tools, the elastic behaviour of unconsolidated rocks is first investigated experimentally by quasi-static and dynamic stress-strain experiments yielding the Young's modulus, nonlinear resonance shift and analysis of harmonic generation. In addition, the transmission of structural waves through granulates is investigated by assessing the transfer function for different thicknesses of granulates, different particle sizes and different materials with varying viscous damping. Three granulates are used, small-scale ballast, a gravel, and two sizes of uniform steel spheres. All three materials exhibit a combination of classical and hysteretic nonlinearity where the strain depends on the stress amplitude and history.

A completely new finite element approach is taken to model the hysteretic nonlinearity, based on an existing phenomenological static model. Multiple spring-slider elements with gaps are used, as opposed to implementing a homogenised material model. It is shown that only 50 elements can reproduce the hysteretic nature of the material, which is a significant advantage to a traditional material model requiring the discretisation of the entire ballast volume. Each spring-slider element is parameterised by two springs constants, a yield force and an initial gap. A distribution of these parameters across the 50 elements is found that reproduces the quasi-static stress cycles acquired experimentally. In addition, a parametric study of the model parameters during dynamic excitation reveals that key indicators of nonlinearity can be simulated. The finite element simulations prove that using a set of spring-slider elements to model the behaviour of unconsolidated granulates is viable method. With experimental tests performed on true ballast and further work on the finite element model to understand optimal parameter distributions, a more accurate and efficient railway superstructure model can be produced.

Acknowledgements

Table of Contents

List of Figures

List of Tables

Chapter 1

Introduction

1-1   Unconsolidated granular materials

Understanding the elastic behaviour of unconsolidated granular materials is important due to their abundant presence in nature and man-made applications. One use for this type of material is ballast in railway construction as part of the railway superstructure, this is the crushed granular material used as the structure in which the sleepers are embedded. Railway ballast has many functions, including draining water away from the track, to retain the track in a stable position and to disperse the load from the sleepers onto the underlying material (Selig and Waters, 1994). However, one of the most vital functions of ballast is to provide a medium for the absorption of impact forces caused by passing trains and dissipation of this energy into the surrounding subsurface material (Mundrey, 2009). This feature of ballast is important as it minimises vibrational disturbance to the surrounding areas, therefore it is essential to study how structural waves propagate through the ballast to optimise its energy absorbing properties. In addition, the elastic behaviour of ballast affects the vibrational properties of the railway superstructure, and thereby the acoustic radiation during train pass-by.

Railway ballast is a granular material consisting of irregularly shaped particles of varying size which puts it in the *Structural Nonlinear Elasticity* class (Ostrovsky and Johnson, 2001). The nonlinearity of this class of materials exists from the presence of small soft features of the grain contacts within a hard matrix of the grains. The nonlinear nature of granular media is defined by its response to stress. The elastic moduli of nonlinear materials are dependent on the applied load which results in a nonlinear stress-strain curve. Conversely, the elastic moduli of linear materials are independent of the applied load which results in a linear stress-strain curve (Fig. 1-1a). Nonlinear materials can be split into two subclasses, *classical* nonlinearity and *hysteretic* nonlinearity. Classical nonlinearity is characterised by the stress-strain curve following the same path for loading and unloading (Fig. 1-1b). Hysteretic nonlinearity is characterised by a different stress-strain relation for loading and unloading (Fig. 1-1c). These stress-strain curves form closed loops which shows how these types of materials have a *memory* property with regards to strain (Holcomb, 1981).
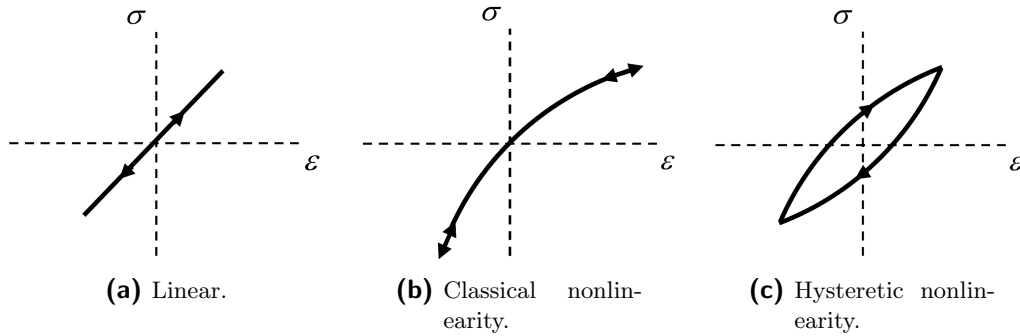
Figure 1-1: Stress (σ) - strain (ε) curves. The arrows denote the stress-strain path (Remillieux et al., 2017).

It has long been known that granular media exhibit a highly nonlinear elastic behaviour. Observations of the response of granular media under quasi-static and dynamic stresses have been used to investigate their nature. Quasi-static measurements involve large strain ($10^{-5} - 10^{-2}$) at low frequency ($10^{-2} - 10^{-5}$ Hz) (Boitnott, 1993) whereas dynamic measurements involve very small strain ($10^{-9} - 10^{-6}$) applied at high frequency ($10^{3} - 10^{6}$ Hz) (Johnson and Rasolofosaon, 1996).

Standardised quasi-static response experiments include uniaxial and triaxial tests that can establish the stress-strain relationship under cyclic loading. These experiments apply loading and unloading to a material using a very small strain rate to have the material in a state of equilibrium which allows inertial effects to be disregarded. The loading and unloading curves are used to gauge material compaction as well as hysteretic curves. Studies have performed uniaxial stress tests on railway ballast using cyclic loading to simulate the passing of trains (Indraratna et al., 1997). These studies have shown railway ballast to exhibit hysteretic nonlinearity when put under stress cycles but also that compaction of the material plays a key role in the stress-strain relationship (Zhai et al., 2004; Indraratna et al., 2009).

One type of dynamic test determines amplitude dependent resonance frequency shift. This experiment applies a frequency sweep to the material at a constant amplitude. This signal is a sinusoid where the frequency is a function of time. The amplitude response of the material to this dynamic signal is dependent on the driving frequency which produces a resonance curve within the frequency range of the sweep. Resonance curves are created for a range of input forces and the comparison between curves can be used to characterise the elastic properties (TenCate and Shankland, 1996). Several studies have performed resonance tests on glass beads (Johnson and Jia, 2005; Inserra et al., 2008; Tournat and Gusev, 2010) which all show that an increasing driving force shifts the resonance peak to lower frequencies. The shift to lower frequencies indicates that the material is becoming softer for larger strain amplitudes, that there is a decrease in the elastic modulus and that there is an increase in attenuation (Tournat and Gusev, 2010). In addition to resonant peak shift with increasing driving force, the resonance peak amplitude decreases and the width of the peak increases. Other studies have performed resonance tests on poorly-consolidated sandstones which produced the same observations as glass beads (Johnson et al., 1996; TenCate and Shankland, 1996).

The creation of harmonics during sinusoidal excitation is another dynamic experiment used as

a standard in the study of nonlinear materials. Harmonic generation requires a monofrequency sinusoidal force to be applied to the material. This excites an oscillation of the same frequency in the material. In nonlinear materials, harmonics will also be generated at multiples of the driving force frequency, where the amplitudes of the 2nd and 3rd harmonics provide the most valuable information (Nazarov et al., 1988). The amplitude response of the 2nd and 3rd harmonics induced in a material are dependent on the strain. This relationship can be used to quantify the nonlinearity of the the material. This relationship is not only found to be linear for poorly-consolidated sandstones, but the gradients of the 2nd and 3rd harmonics are approximately equal (Johnson et al., 1996). Theoretical models have shown that hysteretic nonlinearity produces 2nd and 3rd harmonics with equal slopes (Van Den Abeele et al., 1997).

In addition to exploring the elastic behaviour of granular media, it is also important to investigate how granular media effects wave transmission, especially as a vital role of ballast is to transfer and absorb energy from the pass-by of trains. Granular media have been shown to have a strong influence on the transmission of waves, especially as the movement of grains relative to each other allows for energy absorption. A cut-off frequency exists where the transmission of frequencies above this value is dramatically reduced (Tournat and Gusev, 2009). The cut-off frequency can vary depending on factors such as the particle size and compaction and can play a large role in determining the vibrational properties of energy transmitted into the surroundings.

For linear structures, using the superposition principle, material properties can be scaled linearly. This makes modelling very efficient as switching between scales is simple. Analysis of linear structures can be computed by modal analysis and frequency response calculations to determine what frequencies the structure will resonate at and produce a spectrum of these frequencies. This is not possible for nonlinear materials as the frequency response is amplitude dependent by definition. To solve nonlinear problems, an iterative solver is required which is more computationally expensive. Therefore, it is appealing to model ballast as a linear structure as part of more complex model of the entire railway superstructure. Unfortunately, as ballast is not a linear material, this is a caveat of many railway superstructure models. Several approaches have been made to model the hysteretic nonlinearity displayed by granular media. One approached is called the Preisach-Mayergoyz (PM) framework. This method is a purely mathematical approach and defines multiple features called *hysterons* that result in hysteretic loops, however this framework must be defined for a case by case basis. Another method utilises a model of friction in grain contacts to create hysteretic loops (Iwan, 1966; Aleshin and Van Den Abeele, 2012). Although both of these methods successfully model hysteresis, they are difficult to input into a material model. In addition, both of these methods produce purely hysteretic nonlinearity whereas granular media display a combination of both classical and hysteretic nonlinearity.

Since the implementation of railway ballast in previous models is poor, the outcome of this thesis is therefore to create a more realistic model for granular media than can be implemented in a railway superstructure finite element (FE) model. The results of experimental data on true ballast can be implemented in the FE model where a more accurate representation of how the railway superstructure behaves can be predicted.

1-2   Thesis objectives and outline

To explore the elastic properties of granular materials, this thesis will investigate how elastic waves propagate through this type of material and how they are transmitted into the surrounding subsurface. This will be accomplished by splitting the thesis into two parts, the first part will deal with the elastic behaviour and the second part will deal with wave transmission. Both parts will involve acquiring experimental data from granular media where the nonlinear properties will be investigated. Finally, the experimental data will be implemented in a Finite Element model.

For this purpose, the following tasks are completed in the framework of this thesis:

- Acquire data from dynamic and quasi-static stress tests.

- Analyse acquired data from experiments to characterise the nonlinearity of granular material.

- Analyse experimental data of wave transmission.

- Design a finite element model to simulate behaviour of granular material.

- Compare results of finite element model to acquired data.

- Investigate how finite element model improves traditional models.

This thesis will begin with an introduction to the nonlinear behaviour of elastic materials, including a straightforward theoretical model of nonlinearity and an outline of the predictions of nonlinear behaviour in Chapter 2. Chapter's 3 and 4 detail experimental studies of elastic behaviour in the quasi-static and dynamic regimes, respectively, and Chapter 5 details a study into wave transmission. In Chapter's 3, 4 and 5, a description of the apparatus and test procedure is given followed by the results and a short discussion for each test. How the finite element model is assembled is explained in Chapter 6 including background information on the physics of the model. Chapter 7 discusses the overview of the entire thesis and an outlook of the work that should be done moving forwards.

Chapter 2

Nonlinear elastic behaviour of granular media

2-1 Introduction

The existence of nonlinear elastic materials has been known for several decades. More specifically, it has long been known that granular media fall into this category as they have a strong nonlinear component and exhibit hysteresis when stress cycles are applied. Granular media have a bond system of grain contacts, movement of the grains relative to each other produces nonlinearity and hysteresis results from friction at the grain contacts. These effects have been well documented and the reasons why they occur investigated.

In this chapter, an introduction to nonlinear behaviour will be given. This will consist of stating a theoretical model for nonlinearity, based on a stress-strain relationship, and will describe predictions resulting from this model. Previous work done to capture hysteretic behaviour will be outlined. A physical model consisting of spring-slip will be given that demonstrates hysteretic nonlinear behaviour. Key indicators of nonlinearity in a material are presented from quasistatic and dynamic data acquired from laboratory experiments. These indicators are not only used to give qualitative information but can also provide quantitative measures of the nonlinearity. The chapter will conclude with a description of damping and prediction of wave transmission through granular material.

2-2 Stress and strain

Stress describes the force per unit area that is exerted in a continuous medium. *Strain* describes the change in length of a continuous medium that is under the exertion of stress and is a dimensionless quantity.

Stress, ε, is calculated from the force, F, and the cross-sectional area, A

$$\sigma = \frac{F}{A}.$$ (2-1)

Strain is calculated from the displacement, ΔL, divided by the original length of the sample, L

$$\varepsilon = \frac{\Delta L}{L}. \tag{2-2}$$

An important elastic modulus, the Young's Modulus, E, is derived from the relation of stress and strain

$$E = \frac{d\sigma}{d\varepsilon}. \tag{2-3}$$

In linear materials, the Young's Modulus is constant, E_0, and the material obeys Hooke's Law

$$\sigma = E_0\varepsilon. \tag{2-4}$$

Theoretical models to quantify nonlinear behaviour have been proposed for both classical and hysteretic behaviour. These models are called Equations of State (EOS) and are derived using an energy expansion (McCall, 1994). For classical nonlinearity the relation of stress, σ, to strain, ε, is

$$\sigma = E_0(\varepsilon + \beta\varepsilon^2 + \delta\varepsilon^3 + ...), \tag{2-5}$$

where E_0 is the linear Young's Modulus at infinitesimally small strain while β and δ are the 1st and 2nd nonlinear coefficients respectively. Higher order nonlinear parameters are possible, however they are not very frequent. The equation for hysteretic nonlinearity is the same as for classical nonlinearity but an additional term is present which describes hysteretic effects

$$\sigma = E_0(\varepsilon + \beta\varepsilon^2 + \delta\varepsilon^3) + f[\varepsilon, \text{sgn}(\dot{\varepsilon})], \tag{2-6}$$

where f is a function of strain and the sign of the strain rate. The sign of the strain rate equals +1 for loading and -1 for unloading, the presence of this function allows a different stress-strain relation for loading and unloading. For a cyclic stress function, the hysteretic function can be described by the following first order equation

$$f[\varepsilon, \text{sgn}(\dot{\varepsilon})] = -\alpha E_0[\Delta\varepsilon + \varepsilon\text{sgn}(\dot{\varepsilon})], \tag{2-7}$$

where α is a constant describing hysteretic effects and $\Delta\varepsilon$ is the amplitude during the last stress period.

Using these models of linearity, classical nonlinearity and hysteretic nonlinearity, we can predict the effect of applying a monofrequency sinusoidal signal to these types of materials. By simulating the time series of the propagating waves, three distinct observations are shown for the three elastic behaviours. For linear materials, a propagating sinusoidal wave will keep its shape (Fig. 2-1a). In the case of classical nonlinearity, the propagating sinusoid evolves to become highly asymmetric (Fig. 2-1b), whereas in the hysteretic case, the propagating sinusoid evolves into a triangular wave (Fig. 2-1c).

(a) Linear.   **(b)** Classical nonlin-earity.   **(c)** Hysteretic nonlin-earity.
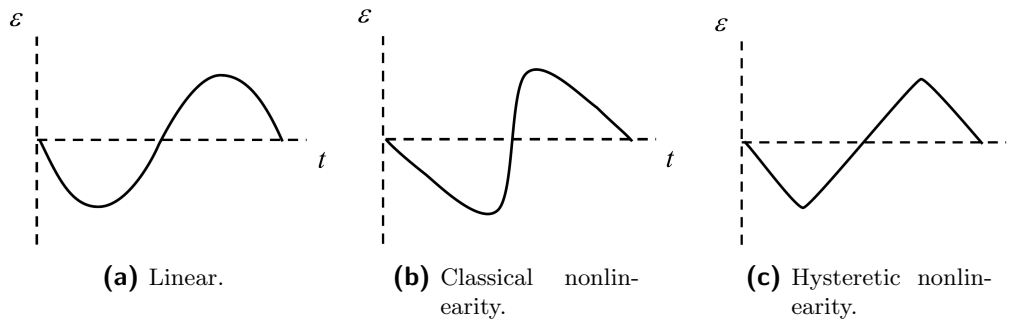
Figure 2-1: Strain (ε) time series (Remillieux et al., 2017).

The nonlinear distortion of sinusoidal waves can be easily noticed in the frequency domain. In linear materials, the amplitude spectra only have one peak at the same frequency as the input signal (Fig. 2-2a), whereas nonlinear behaviour results in additional peaks at multiples of the input frequency called *harmonics*. More specifically, classical nonlinearity will induce harmonics at every multiple of the input signal (Fig. 2-2b) but purely hysteretic behaviour will only induce harmonics at odd multiples of the input frequency i.e. odd harmonics (Fig. 2-2c). The generation of these types of harmonics explains why propagating sinusoids are deformed asymmetrically and into triangular waves respectively for classical and hysteretic nonlinearities (Remillieux et al., 2017).

(a) Linear.   **(b)** Classical nonlin-earity.   **(c)** Hysteretic nonlin-earity.
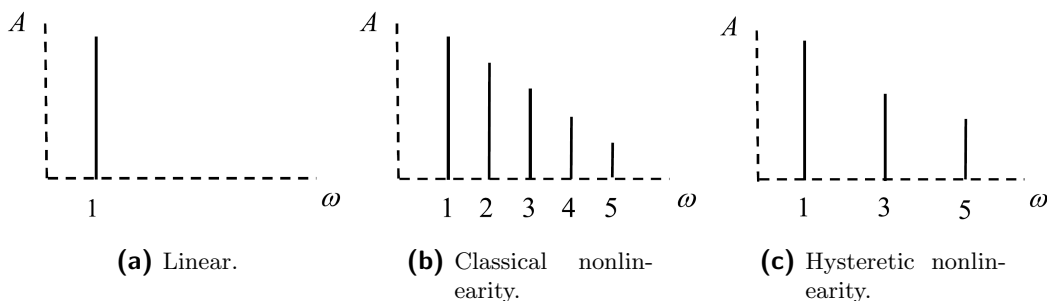
Figure 2-2: Strain (ε) amplitude spectrum (Remillieux et al., 2017).

2-3   Hysteretic models

2-3-1   Hertzian friction modelling of hysteresis

Physical explanations of nonlinearity have been attributed to friction between grains of the material (Gist, 1994). In particular, hysteresis is attributed to stick-slip motion due to this friction at the grain contacts Aleshin and Van Den Abeele (2012). Considering an individual contact, the forces at this contact can be resolved.

If we consider an isotropic elastic sphere with radius, R, that is forced against a flat surface with force, N, as shown in Figure 2-3, the force that arises at the contact is due to the

excess material of the sphere that would be below the flat surface if the material was absent. The volume, δV, of the sphere that would be below the flat surface approximately equals $a^2 h$ where $a = \sqrt{Rh}$ is the surface area of the contact and h is the distance the sphere would have intruded the flat surface if the material was absent. The strain in this volume, $\varepsilon \approx \delta V/a^3 \approx h/a$, produces a pressure $P \approx K\varepsilon \approx Kh/a$ that pushes down on the contact area. Thus the force, N, on the contact surface is given by

$$N \approx Pa^2 \approx Kah \approx K\sqrt{Rh^3}. \tag{2-8}$$

If the sphere is pushed against a flat surface with force, N, and then a shearing force, T, is applied, assuming no slip at the contact occurs, the surface area of the contact is unchanged. As a displacement, Δs, builds up across the volume, shear strain $\Delta s/a$ will be produced. Therefore

$$T \approx a^2 \tau \approx \mu a \Delta s, \tag{2-9}$$

where τ is the traction. Equations 2-8 and 2-9 describe a Hertz-Mindlin contact.
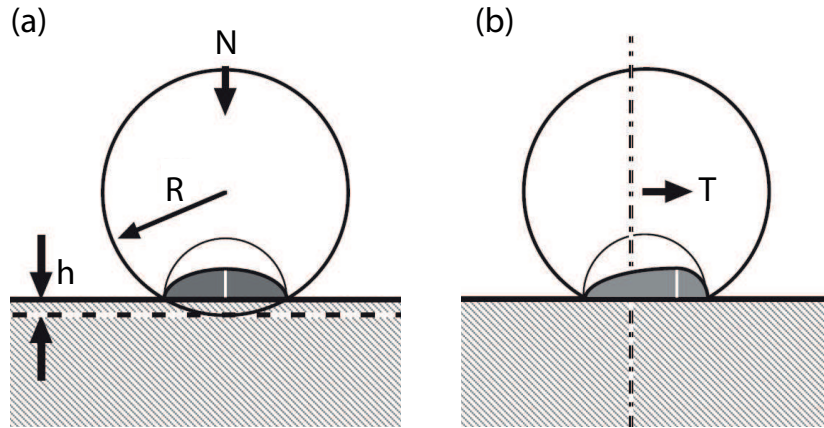
Figure 2-3: Hertzian contact of a sphere on a flat surface during normal stress (a) and shear stress (b) (Guyer and Johnson, 2009).

The Hertz-Mindlin model first applies a normal compression to the contact and then a tangential force is applied afterward (Mavko et al., 2009). This shear force may induce slip at the contact which depends on the coefficient of friction between the contacting bodies. In granular media, the contact will be between two particles with convex surfaces, for model simplicity we assume all particles are identical spheres. It can be shown that the radius of the contact area is given by

$$a = \left[\frac{3F_c R}{8\mu}(1 - v) \right]^{1/3}, \tag{2-10}$$

where F_c is the confining force, μ and v are the shear modulus and Poisson ratio of the sphere material, respectively.

Now the frictional component of the contact can be used to model hysteresis. Aleshin and Van Den Abeele (2012) used the stick-slip motion of Hertz-Mindlin contacts to produce motion that has *memory*. An algorithm is created that consists of a sequence of stick-slip boundaries. The position of these boundaries and their history are stored by the *system memory*. The movement along these boundaries is dependent on the normal and tangential forces. The foundation of this approach is analytical with different modes of the stick-slip boundaries that represent different stick-slip regimes. The stick-slip boundaries are used to create a *memory diagram* which allows the entire complexity of the analytical formulas to be reproduced by a simple evolving hysteretic diagram. This is good for understanding the role the contacts play but makes it difficult to implement as a material property in a Finite Element solver as modelling each individual contact is unnecessary.

2-3-2 Preisach-Mayergoyz framework

One approach to modelling hysteresis quantitatively is described by the Preisach-Mayergoyz (PM) framework (Preisach, 1935; Mayergoyz, 1985). The approach taken by this model is to describe a material as a collection of *hysterons*. An individual hysteron represents a single stress-strain state and a conglomeration of them can be used to exhibit hysteretic behaviour. Hysterons can either be in an open or closed state. The stress value required for opening and closing of a hysteron is represented by σ_o and σ_c, respectively, and these values can be differ between hysterons. When a single hysteron is opened or closed, the strain is taken to be a constant value, γ (Fig. 2-4a). All defined hysterons can be distributed in a space defined as a function of σ_o and σ_c called the PM space. As $\sigma_c \geq \sigma_o$, the PM space is defined by a triangular zone bounded by $\sigma_o = \sigma_c$ (Fig. 2-4b). The zone should theoretically exist infinitely beneath this bound but it is limited by a minimum σ_o and maximum σ_c for practical calculations.
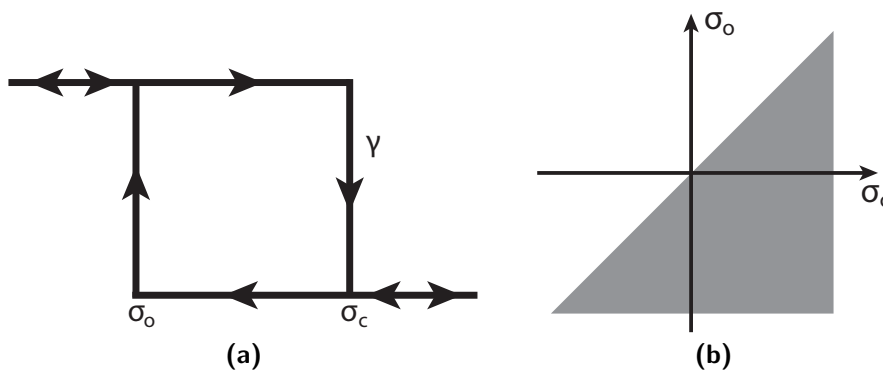
Figure 2-4: An individual hysteron (a) and PM space distribution (b).

The distribution of hysterons is done mathematically using a density function. As hysteretic materials have a different value for strain at a given stress depending on the load direction, the strain value cannot be read directly from the stress value. Using the PM framework, the total strain can be calculated from how many hysterons are open at a given point in the loading curve. For a given stress history, a bookkeeping of the open and closed hysterons can be made. The total macroscopic strain equals the number of open hysterons multiplied by the hysteron strain value, γ.

The PM framework being a mathematical tool makes it difficult to predict the hysteron density fucntion based on physical reality. In addition, this method is a purely hysteretic model that only accounts for hysteretic nonlinearity and not classical nonlinearity. This is problematic for modelling of a physical materials which show a combination of classical and hysteretic nonlinearity.

2-3-3   Spring-slider models

An alternative method to simulate hysteretic behaviour is to create a mechanical model consisting of springs and sliders that is physically motivated. Iwan (1966) presents a model consisting of a series of elastoplastic elements that produce hysteretic loops under stress cycles. The model uses multiple linear spring-slider elements with a total spring constant of k. Each spring-slider element consists of linear spring in series with a slider that activates at the sliding force, f^S (Fig. 2-5). The slider prevents the force, f, increasing further with any additional displacement.
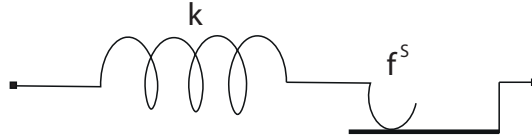
Figure 2-5: Anatomy of spring-slider element.

If we only consider one spring-slide element, the initial force-displacement curve will take the form of Hooke's Law

$$f = kx; \ \dot{x} > 0, \ 0 \leq x \leq \frac{f^S}{k}. \tag{2-11}$$

The element yields when the force reaches the sliding force

$$f = f^S; \ \dot{x} > 0, \ x \geq \frac{f^S}{k}. \tag{2-12}$$

When the direction of loading is reversed after the element has yielded, the force-deflection curve will follow the same gradient as the initial loading curve

$$f = kx - (kA_{x+} - f^S); \ \dot{x} < 0, \ A_{x+} - \frac{2f^S}{k} \leq x \leq A, \tag{2-13}$$

where A_{x+} is the maximum displacement during $\dot{x} > 0$. The element also yields in the negative displacement direction at the negative of the sliding force

$$f = -f^S; \ \dot{x} < 0, \ x \leq A_{x+} - \frac{2f^S}{k}. \tag{2-14}$$

When the direction of loading is reversed again, the force-displacement curve still has the same gradient as the initial loading curve

$$f = kx - kA_{x-} + f^S; \ \dot{x} > 0, \ A_{x-} \leq x \leq A_{x-} + \frac{2f^S}{k}. \tag{2-15}$$

The element will yield again according to Eq. (2-12) and the process of loading and unloading can be repeated indefinitely. If the maximum displacement of loading and unloading is equal, i.e. $|A_{x+}| = |A_{x-}|$ then the force-displacement curve will follow the same loop (Fig. 2-6).
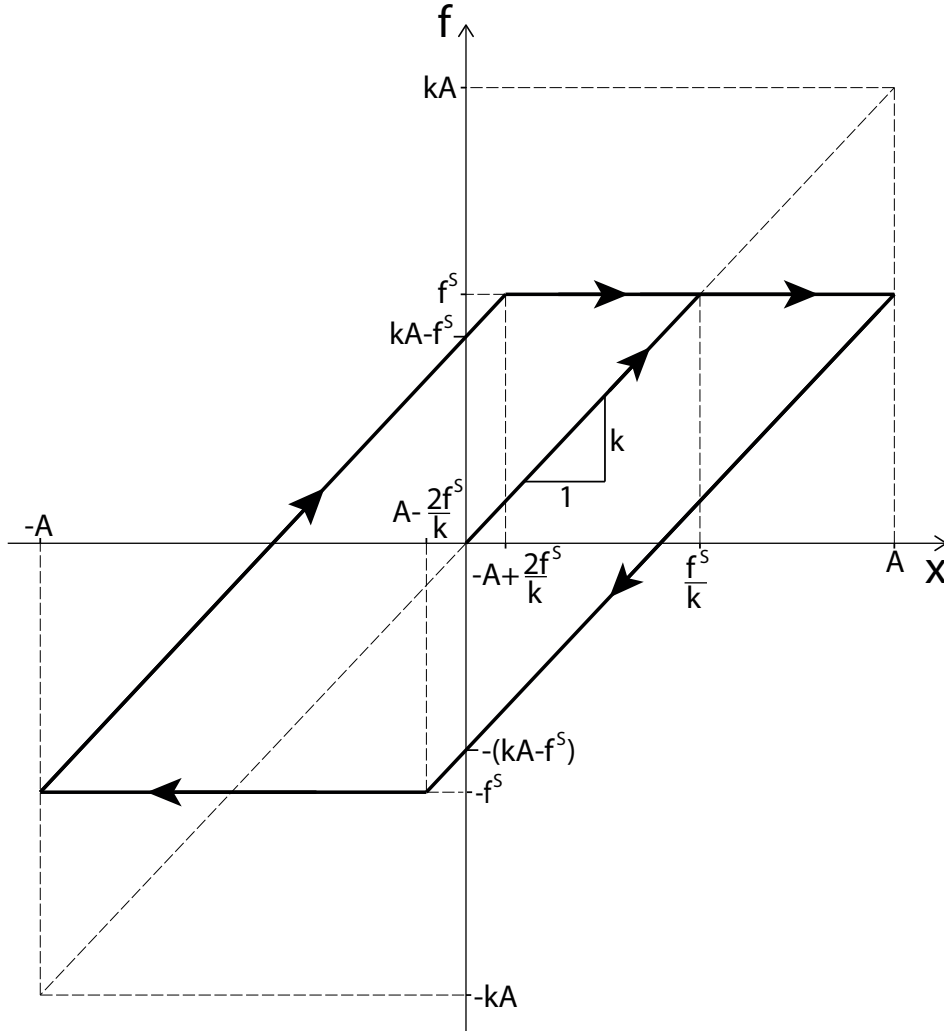
Figure 2-6: Force-displacement curve for a single spring-slider element.

If N of these spring-slider elements are placed in parallel (Fig. 2-7), the sum of all spring constants will equal

$$k_{total} = \sum_{i=1}^{N} k_i. \tag{2-16}$$

By using a range of values for f^S, the resultant hysteretic loop will become curved as different spring-slider elements yield at different displacements (Fig. 2-8). The values for f^S are set by a function. If a linear distribution is required, a parameter β can be used. f_1^S will equal $(1 - \beta)f^S$ and f_N^S will equal $(1 + \beta)f^S$. The remaining values for f_i^S will be evenly spaced between these two bounds for the linear distribution.

Using springs to model material properties has the advantage of being a relatively simple method to recreate complex hysteretic behaviour. In addition, the behaviour of the spring-slider can be compared to the stick-slip motion at a grain contact. The behaviour of these elastoplastic elements is purely hysteretic, classical nonlinearity can be introduced by using a nonlinear spring.

Unlike the PM model, each elastoplastic element can be modelled independently, which makes it very suitable for finite element models. The difficulty lies in the choice of the spring constants and yield forces, so that the model reproduces experimental results.
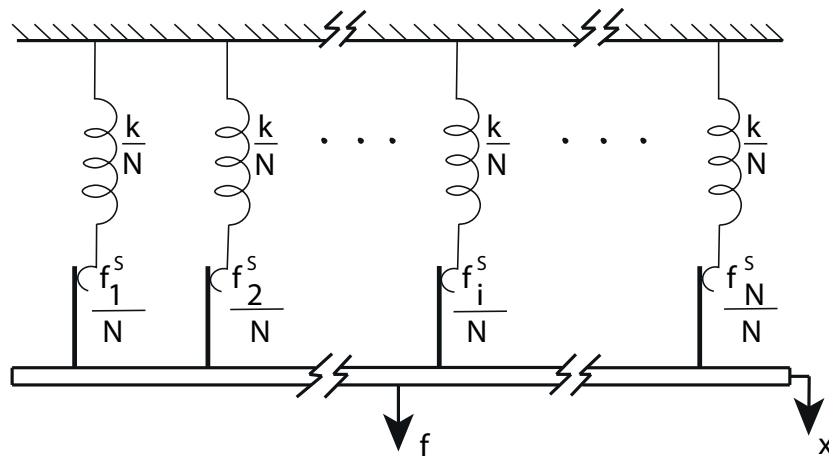
Figure 2-7: Multiple spring and slider elements in parallel.
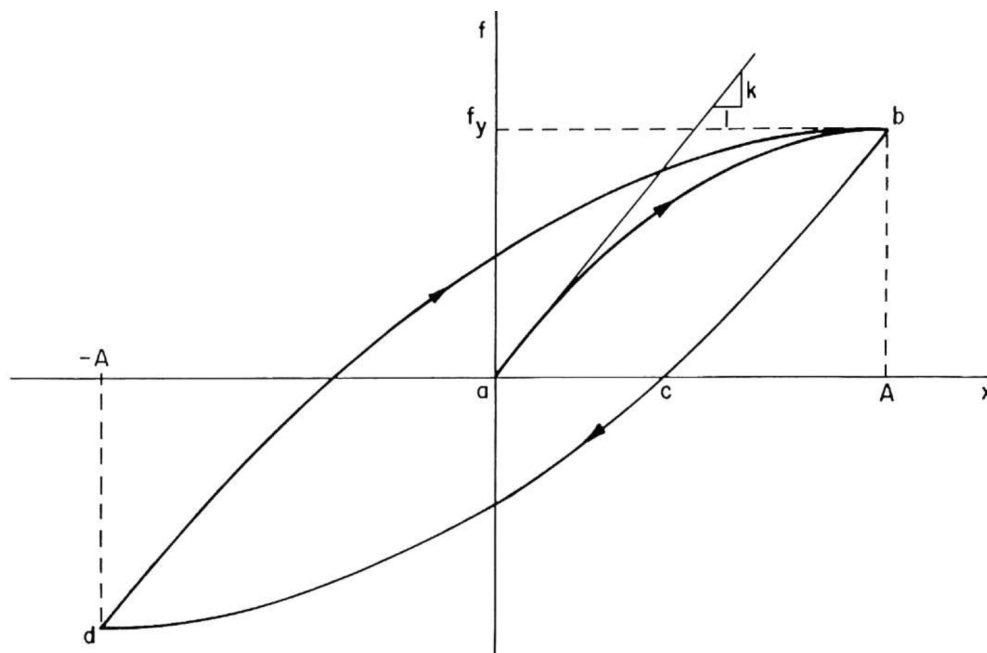
Figure 2-8: Hysteretic loop formed by multiple spring and slider elements in parallel (Iwan, 1966).

2-4   Key experimental indicators of nonlinearity

2-4-1   Quasi-static stress-strain experiments

The most obvious indication of nonlinearity in a material comes from observations of quasi-static loading. Quasi-static stress-strain measurements are a standardised experimental method where the displacement rate is slow enough that effects of inertia are negligible. This assumes that the system remains in equilibrium and time has no effect. Quasi-static stress-strain experiments typically apply a uniaxial stress to a material and measure the strain in the same direction that the force is applied. Such experiments reveal certain characteristics of nonlinear materials, such as a nonlinear stress-strain curve, different stress-strain relation for loading and unloading (i.e. hysteresis) and end point memory.

A nonlinear stress-strain curve is crucial to consider as the derivative of stress with respect to strain, $d\sigma/d\varepsilon$, equals the Young's Modulus. Hysteretic behaviour shown by stress-strain loops shows how the system is dependent on the strain history which is related to end point memory. If a partial stress cycle is completed during a full stress cycle, a smaller stress-strain loop is formed inside the loop of the full stress cycle. The small loop will always start and end on the inside of the large loop as memory of the previous maximum strain rate is retained. Guyer et al. (1997) apply a quasi-static stress loop to a Berea sandstone with 8 partial loops in the full load cycle. This results in a single, large, closed stress-strain loop and eight small loops that are generated as the large loop is traversed (Fig. 2-9).
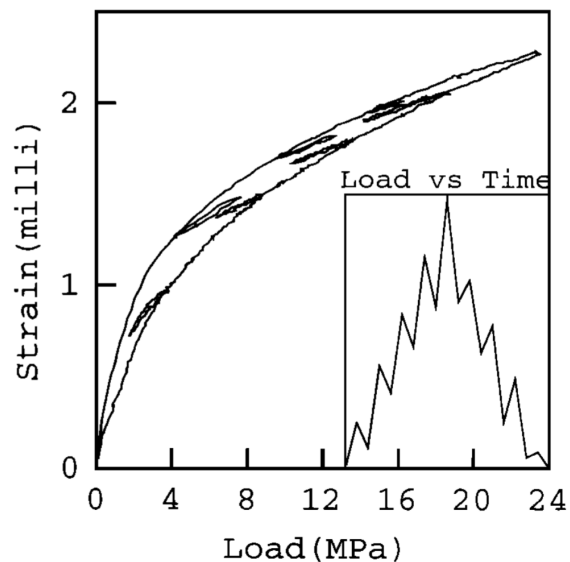
Figure 2-9: Stress-strain curve displaying end point memory (Guyer et al., 1997).

2-4-2   Resonance

Resonance is a phenomenon where the oscillations of a vibrating system increase in amplitude at specific frequencies. When damping is small, the resonance frequency of a material is the frequency that it naturally vibrates. If a material is forced to vibrate at or near to

this frequency, the amplitude of the oscillations will rapidly increase with the peak amplitude occurring at the resonance frequency (also called the *eigenfrequency*). The increase in amplitude is due to the material being able to store energy more easily, therefore the applied force is not dissipated and adds to the amplitude of the oscillations. There are several different modes of resonance that result in different oscillation shapes. These mode shapes are easier to visualise when described in terms of a spring. A common type is the longitudinal mode, this is where the oscillations result in extension and compression of the spring only in the axial direction (Fig. 2-10a). Another resonance mode shape are bending modes which are the side to side oscillations which occur, for example, when you tap the side of a spring fixed at one end (Fig. 2-10b).
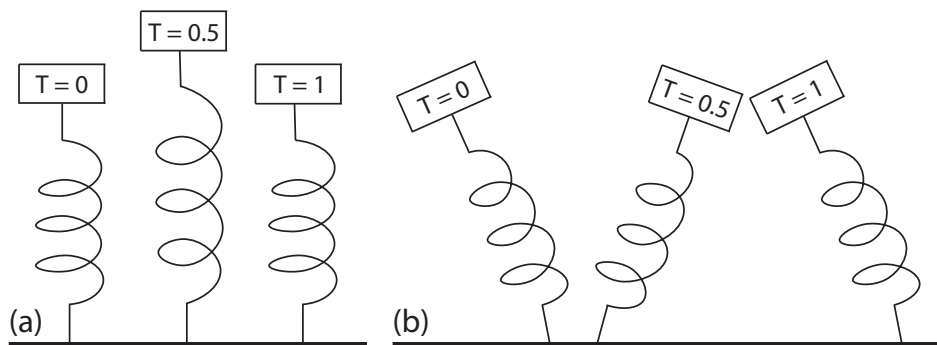
Figure 2-10: Longitudinal (a) and bending (b) mode shapes at 0, 0.5 and 1 period(s).

In a linear material, when the amplitude of the forced vibrations changes, the resonance frequency remains constant. On the other hand, the resonance frequency of a nonlinear material shifts when the amplitude of the forced vibration is changed. Figure 2-11 displays the shift in resonance curves. The amplitude of the spectra has been normalised to the peak amplitude at small driving amplitude. The normalised amplitude decreases as the drive amplitude increases due to higher losses.
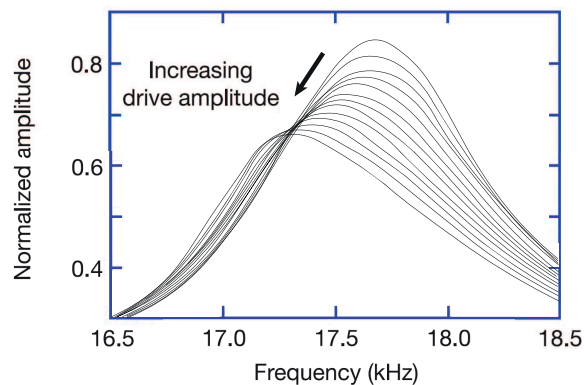
Figure 2-11: Nonlinear resonance curves for increasing drive amplitude. Reproduced from John-son and Jia (2005).

By using the relative change in the eigenfrequency for multiple input amplitudes, a relationship can be established. For 1st order hysteretic nonlinearity, the following equation can be derived

$$\frac{\Delta f_0}{f_0} = \frac{f_0 - f_{res}}{f_0} = \Gamma \Delta \varepsilon, \tag{2-17}$$

where f_{res} is the eigenfrequency, Γ is a constant, $\Delta \varepsilon$ is the maximum strain in the previous stress cycle and f_0 is the eigenfrequency at an infinitesimally small strain given by

$$f_0 = \lim_{\Delta \varepsilon \to 0} f_{res}. \tag{2-18}$$

When the driving amplitude is constant, for example, when a sinusoidal signal is applied, $\Delta \varepsilon$ is the strain amplitude. Figure 2-12 shows the relative frequency shift against the strain amplitude for four rock types excited at different driving amplitudes. All four rock types show a linear relationship between strain amplitude and eigenfrequency which is an indicator of hysteretic nonlinearity (Ostrovsky and Johnson, 2001).
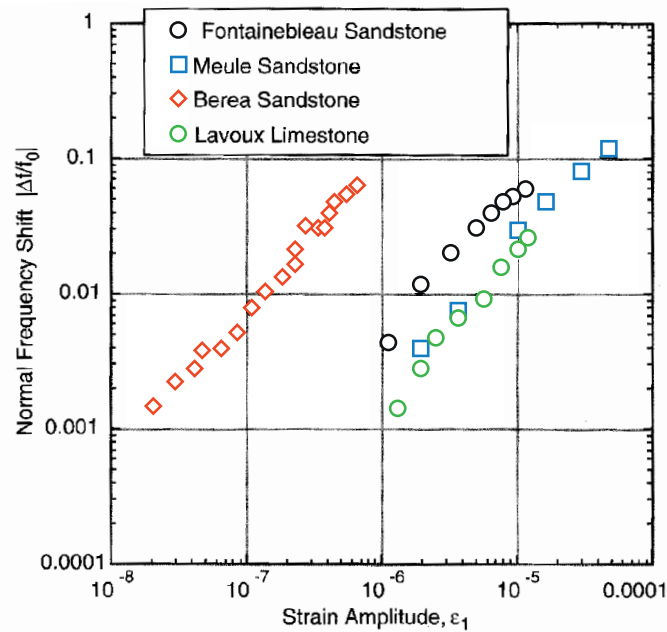
Figure 2-12: Normalised frequency shift vs. strain amplitude (Ostrovsky and Johnson, 2001).

The resonance frequency is an important structural property to obtain, as elastic moduli can be derived from it. If a test material is structured as a simple shape such as a rod or cylinder, when it is resonating, the material can be assumed to behave as a simple harmonic oscillator i.e. the material acts like a spring obeying Hooke's Law. Under this assumption, the resonance frequency, f_0, can be related to the stiffness, k, through the following equation

$$f_0 = \frac{1}{2\pi} \sqrt{\frac{k}{m}}, \tag{2-19}$$

where m is the mass. The stiffness is related to the Young's modulus, E, of the material

$$E = \frac{kL}{A},\tag{2-20}$$

where L is the length of the material and A is the cross-sectional area of the sample. The previous two equations can be equated for k to obtain the Young's modulus directly from the resonance frequency

$$E = \frac{m(2\pi f_0)^2 L}{A} = \frac{m\omega^2 L}{A},\tag{2-21}$$

where ω is the angular frequency.

It can be seen from Eq. (2-21) that the Young's modulus is a function of the resonance frequency, thus as the Young's modulus changes with a change in amplitude in a nonlinear material, the eigenfrequency must also shift.

2-4-3   Generation of harmonics

As mentioned earlier in this chapter, harmonics are oscillations at a multiple of the input frequency. Harmonics are only generated in nonlinear materials and their presence is used as a key indicator of nonlinearity in a material. Figure 2-2 shows how the type of nonlinearity effects the harmonics generated. Pure theoretical classical nonlinearity predicts that both even and odd harmonics will be generated and true hysteretic nonlinearity predicts that only odd harmonics will be generated (Remillieux et al., 2017). The effect of changing the amplitude of the input frequency can also be predicted. The results of this analysis are commonly presented in a plot of harmonic amplitude vs. strain amplitude.

Van Den Abeele et al. (1997) creates three theoretical models based on Equation (2-6) using inputs for β and δ, the nonlinear coefficients as well as a hysteretic parameter, ρ_B. Two of the models are classical nonlinearity, one with only the first nonlinear coefficient and the other with the first two nonlinear coefficients present. The third model is for hysteretic nonlinearity. The amplitudes of the 2nd and 3rd harmonics are calculated for a range of displacement amplitudes for these three models (Fig. 2-13). The results show a linear trend on a logarithmic plot. The slope for classical nonlinearity differs between the 2nd and 3rd harmonics, whereas for hysteretic nonlinearity the slopes for the 2nd and 3rd harmonics are equal. These observations can be transferred to real observations to give a qualitative insight on the linearity. To retrieve quantitative information on the nonlinearity, the value of the harmonic slopes are used. The slope relates to the value of the nonlinear coefficients used for the theoretical stress-strain models.
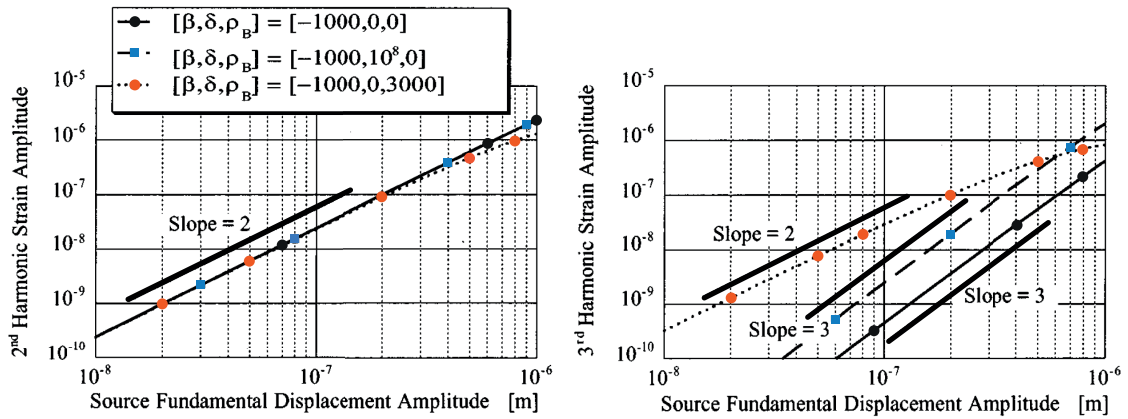
Figure 2-13: 2nd and 3rd harmonic ampltitude vs. strain amplitude of thre model materials. Reproduced from Van Den Abeele et al. (1997).

Figure 2-14 shows experimental data of the the second and third harmonic amplitude against strain amplitude for Berea sandstone (Ostrovsky and Johnson, 2001). The results are sub-parallel with a slope approximately equal to 2. This qualitatively indicates hysteretic behaviour as predicted in Figure 2-13.
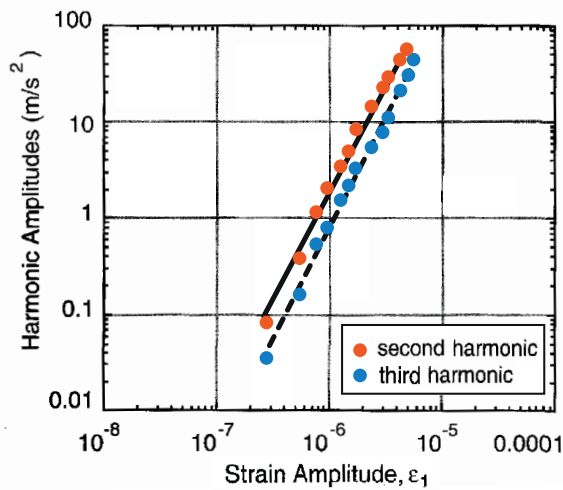
Figure 2-14: 2nd and 3rd harmonic ampltitude vs. strain amplitude of Berea sandstone. Reproduced from Ostrovsky and Johnson (2001).

2-5   Transmission through granular media

A part of this thesis will focus on how waves propagate through granular media. Railway ballast plays a vital role to transfer energy from the pass-by of trains into the surrounding medium. Granular media are suitable for this role, especially due to their nonlinear behaviour and damping. Damping is caused by processes within the system that dissipate the energy of the excitation forces. Inherent damping is dependent on the bulk material property, energy

losses here arise from flex in the material itself. Another type of damping is hysteretic damping. In granular media, this arises from frictional-slip motion of the grain contacts leading to energy losses. Hysteretic damping can be quantitatively calculated from a force-displacement hysteretic loop where the area of the loop equals the energy loss per unit cycle in Joules (Fig. 2-15).
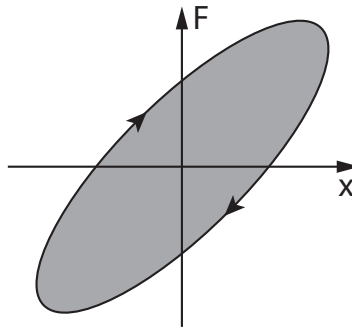
Figure 2-15: Energy loss from hysteretic damping. The area of the grey shaded region equals the energy loss per unit cycle.

The movement of contacts due to travelling energy leads to energy losses, and contributes to frequency dependent attenuation. One clear observation in the frequency response of propagating wavetrains is a cut-off frequency where the amplitude of frequencies above this value are dramatically reduced. Inserra et al. (2008) excites glass beads with a ultrasound transducer to see the effects on the cut-off frequency of changing particle diameter and compaction (Fig. 2-16). The cut-off frequency is increased with decreasing particle diameter and it is decreased with increasing compaction. Below the cut-off frequency, the energy has been shown to be mostly associated with energy travelling through the particles and their contacts (Tournat and Gusev, 2010). Energy above the cut-off frequency is mostly associated with acoustic waves travelling through the pore space material, air in this case. However, only the first regime is important as we are only looking at the solid frame and excitation will be done with a direct force not a transducer.
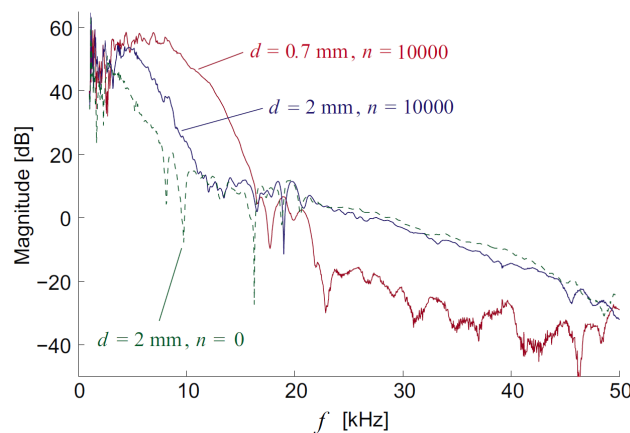
Figure 2-16: Transfer function of a 8 cm thick layer of glass beads for different bead diameter, d, and different number of applied mechanical taps, n (Tournat and Gusev, 2010).

Chapter 3

Experimental study of the quasi-static behaviour of unconsolidated granulates

3-1   Introduction

The previous chapter described methods to quantify the nonlinearity of materials. In this and the next chapter, both static and dynamic methods are implemented for several unconsolidated granulates. To produce a realistic Finite Element model of granular material, input parameters must be obtained from tests on the material to be modelled.

In this chapter, quasi-static stress cycles are completed to obtain material behaviour under low strain rate without inertial effects. The quasi-static tests allow a much larger stress to be applied compared to the dynamic tests as the strain rate is much lower. The quasi-static tests also allows for a precompression to be applied to the material before loading begins to see what effect this has on the response of the material. The apparatus and set-up will be described and give a description of the test procedure. The results are also given followed by a discussion.

3-2   Test material

The unconsolidated granulate used for the quasi-static experiment is a scaled down sample of railway ballast, referred to here as *gravel* (Fig. 4-1a). Typically, railway ballast is roughly 40 - 70 mm in diameter (Indraratna et al., 1997) but the gravel used is approximately 5 - 20 mm in diameter. This material was chosen as it allows easier handling during the experiments and retains the highly angular and rocky nature of typical railway ballast. The bulk properties of the gravel are listed in Table 3-1.

Figure 3-1: Small-scale railway ballast, *gravel*.

Table 3-1: Bulk properties of the gravel.

Parameter	Gravel
Material	Crushed rock
Young's Modulus [GPa]	20
Density [kgm^{-3}]	2400
Particle diameter [mm]	5 - 20

3-3 Apparatus and procedure

The gravel is contained within a 150 mm high hollow steel cylinder with an internal diameter of 98 mm. A cylindrical mass with a diameter of 45 mm and mass of 1.482 kg is placed on top of the gravel, making sure it is not in contact with the inside of the cylinder. A hydraulic press is used (Fig. 3-2) to apply a computer-controlled displacement. A force sensor in the press head allows the force to be measured.

Quasistatic conditions are created by using a very slow strain rate. The press used to compress the gravel in this experiment applies a displacement rate of 1 mm/min. The material is loaded and unloaded for multiple cycles increasing the maximum displacement for each subsequent cycle (Fig. 3-3). The force at the press head is recorded continuously during the experiment.

After the stress cycles have finished, the now compressed material is removed from the cylinder and poured back in loosely. The following tests apply a precompression to the material before the the stress cycles of the previous test are repeated. The method of applying a precompression to the material is repeated for several different forces.
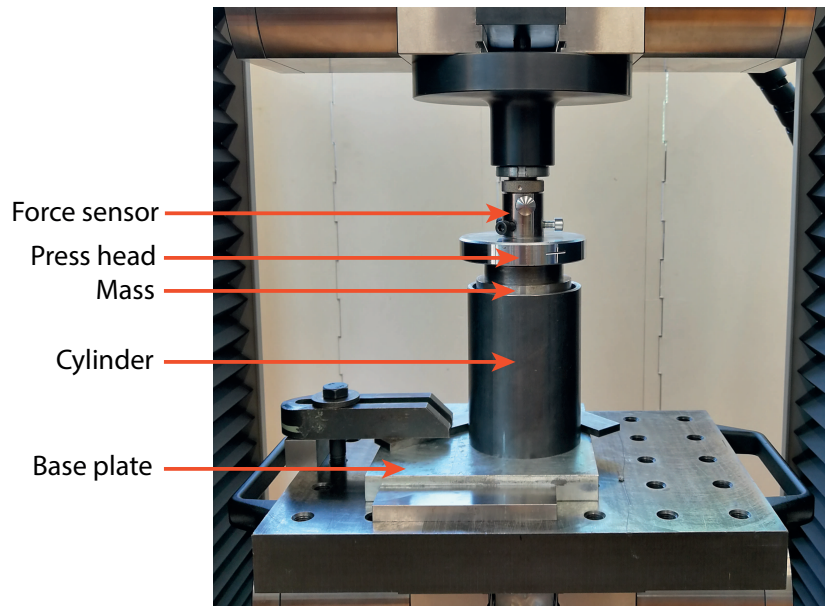
Figure 3-2: Apparatus for quasi-static stress-cycle tests.
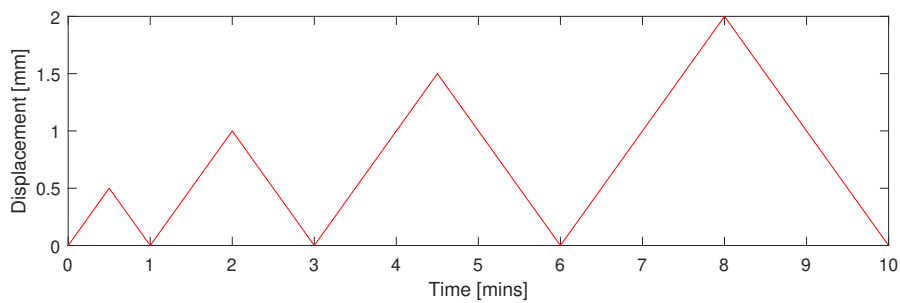
Figure 3-3: Displacement curve applied by the press for the quasi-static tests.

Table 3-2: Parameters for the quasi-static stress cycles.

Parameter	Value
Displacement rate	1 mm/min
Number of stress cycles	4
Displacement amplitude	0.5, 1.0, 1.5 & 2.0 mm
Pre-compression force	500, 1000 & 3000 N

3-4 Results

The mechanical press applies a pre-stress followed by four stress cycles at increasing amplitude (Fig. 4-3). The resulting force and displacement measurements are plotted against each other for the three pre-stresses of 500, 1000 and 3000 N in Figure 3-4. The stress-strain relation for each test is calculated from Equations (2-1) and (2-2).

(a) 500 N.

(b) 1000 N.

(c) 3000 N.
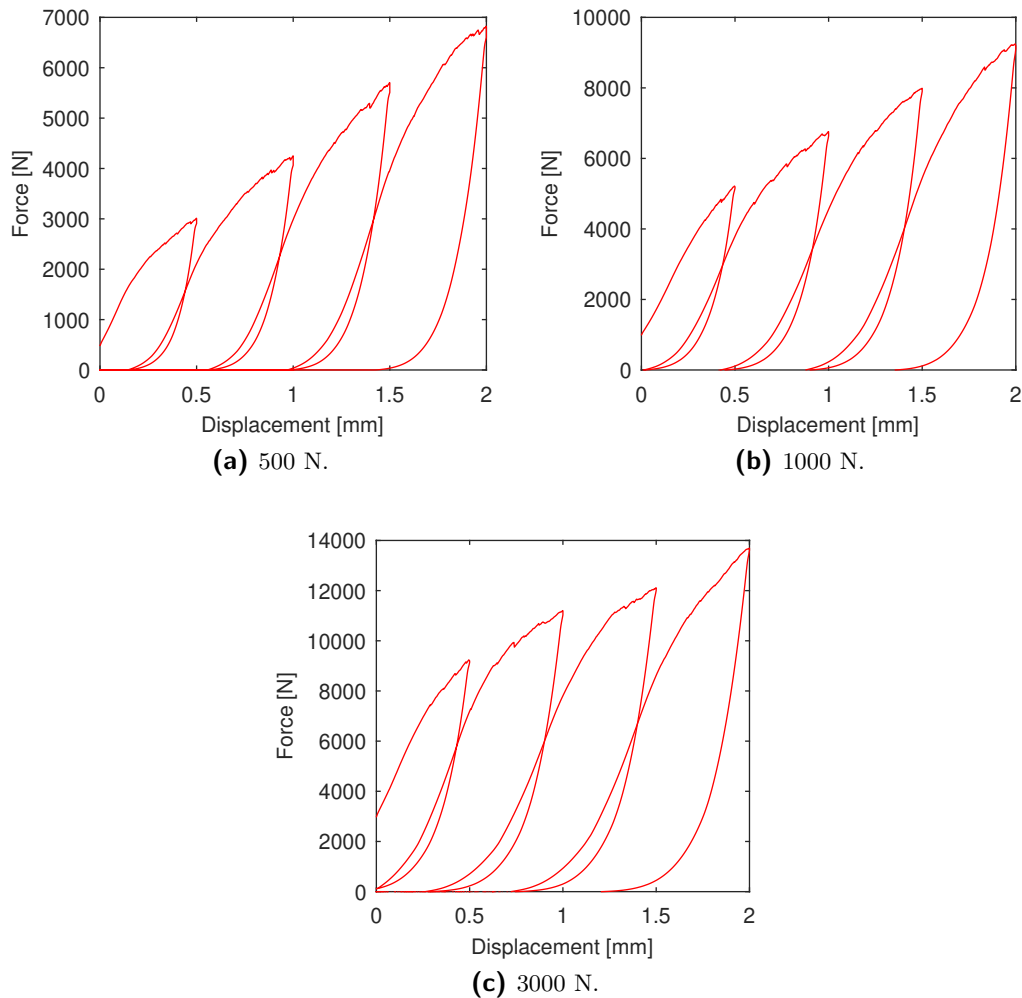
Figure 3-4: Quasi-static stress cycles.

3-5   Discussion

The quasi-static tests produce stress-strain loops that are established in a clockwise direction. When a loop reaches zero force, the displacement is greater than zero which shows that plastic compaction of the material has occurred. At this point during the tests, the displacement will continue to zero with the press head not in contact with the test material. For all tests, the loops reach a higher peak force, as the displacement is higher for each subsequent cycle. As the displacement loop approaches its maximum value, the slope of the stress-strain curve decreases indicating strain softening. Once the maximum displacement is reached and it starts to decrease, the force decreases rapidly resulting in a high stress-strain gradient. The value of the pre-stress does not have an effect on the shape of the stress-strain loops, but does effect the peak force reached during each loop. A larger pre-stress increases the gradient of the stress-strain slopes, thus a higher peak force is reached for the same displacement.

<div align="right">

Chapter 4

</div>

Experimental study of the dynamic behaviour of unconsolidated granulates

4-1   Introduction

Dynamic stress tests are another method to investigate nonlinearity. These are important in the context of this thesis, as train pass-by is a transient occurrence. The resonance frequency shift, harmonic response and dynamic stress-strain curves of granular media are obtained under high strain rate where inertia has to be taken into account. This chapter will describe the apparatus used in the dynamic experiments and give a description of each test procedure. After each procedure, the results are presented along with a discussion.

4-2   Test materials

The gravel used in the quasi-static tests in Chapter 3 is used again for the dynamic tests. In addition, uniform steel spheres are tested to see the results of a different material but these will not be included in the FE models. Two different sizes of steel spheres are used, both 5 and 10 mm diameter (Fig. 4-1). The bulk properties of the steel spheres are listed in Table 4-1.

<div align="center">

Table 4-1: Bulk properties of the steel spheres.

Parameter	5 mm spheres	10 mm spheres
Material	Stainless steel	Stainless steel
Young's Modulus [GPa]	190	190
Density [kgm^{-3}]	7600	7600
Particle diameter [mm]	5	10

</div>
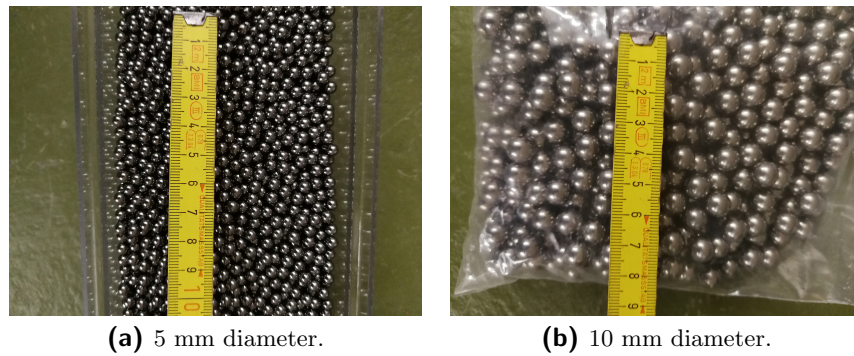
(a) 5 mm diameter.   **(b)** 10 mm diameter.

Figure 4-1: Uniform steel spheres used in the experiments.

4-3   Apparatus and procedure

The test material is contained within the same hollow steel cylinder used for the quasi-static tests. The dynamic excitation is achieved using a shaker. The shaker is attached to a tripod with the vibrating end of the shaker facing down towards the floor. The cylinder is placed on a steel base plate. A cylindrical mass with a diameter of 90 mm is placed on top of the test material so that it is not touching the sides of the hollow cylinder. A force sensor is directly screwed into the centre of the top side of the cylindrical mass which is then attached to the shaker by a stinger. An accelerometer is secured to the top of the mass using bees wax. The set-up is shown in Figure 4-2.

The shaker is controlled electronically using LabView software installed on a laptop. The laptop is connected to a National Instruments PXIe-5402 signal generator and a PXIe-4499 data acquisition card that are synchronised using a PXIe-1073 chassis. The generator is connected to an amplifier which provides the shaker with power. The force sensor and accelerometer are both connected to the data acquisition card.
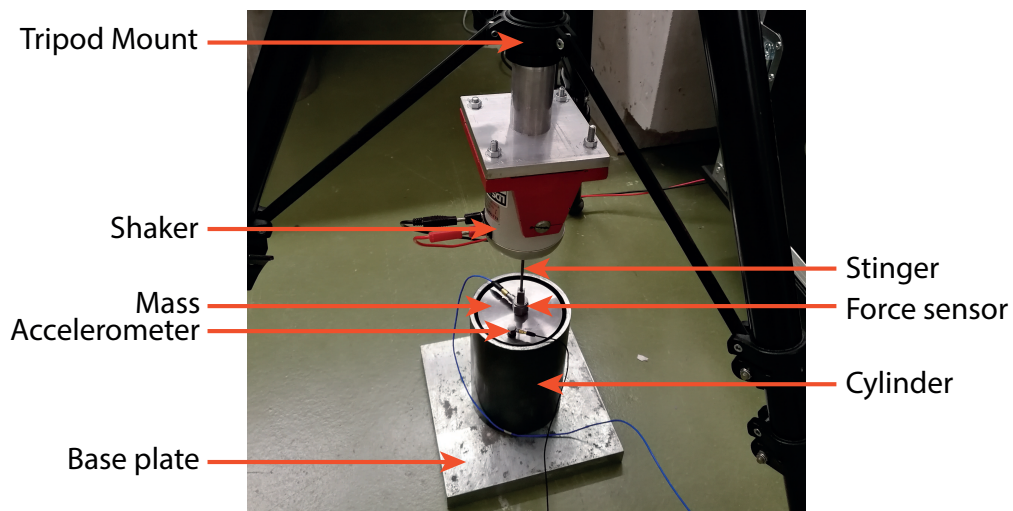
Figure 4-2: Apparatus for contained dynamic tests.

During each test, the material is loosely poured into the hollow cylinder. The mass is placed on top, the sensors are attached and the shaker is connected. The weight of the mass alone is not enough to compact the material. This means that the material will remain in a loose random packing which will start to compact during tests (Knight et al., 1995). Therefore, it is important to first compact the material before any tests are completed, otherwise following tests will be affected. A generator within the LabView software was used to create a ramp-up function at 200 Hz, with an amplitude of 2 V. This was applied to the material for 5 minutes to allow compaction. The material was then left to sit for 2 minutes to allow for relaxation effects (Richard et al., 2005), only then are the dynamic experiments carried out. After each test, the data quality is checked. In the LabView software, the time series data are displayed instantly after acquisition. Data quality checks consist of making sure of the following features in the time series:

- There are no large perturbations, i.e. the signal-to-noise ratio is good.

- There is no DC offset from the x-axis due to defective equipment.

- There is no significant noise in both the force and acceleration data.

- The force sensor is detecting a smooth sinusoidal force time series.

4-4   Dynamic stress-strain curves

4-4-1   Acquisition

Applying dynamic stress cycles to granular media produces hysteretic loops where the inertia effects are present. A monofrequency signal is generated and this force is applied to the material via the shaker. The amplitude of the transient response initially increases before maintaining a constant amplitude (Fig. 4-3). The signal is applied for 0.5 s where the force and acceleration readings are recorded. The measurement time is 0.6 s to allow the motion of the granular material to settle before the next measurement. The measurements are repeated 50 times and they are stacked to increase the signal-to-noise ratio. The experiment is repeated at different input signal amplitudes to produce results for a range of strains. In addition, the response to different amplitudes is measured at three different frequencies. Measurement parameters are stated in Table 4-2.
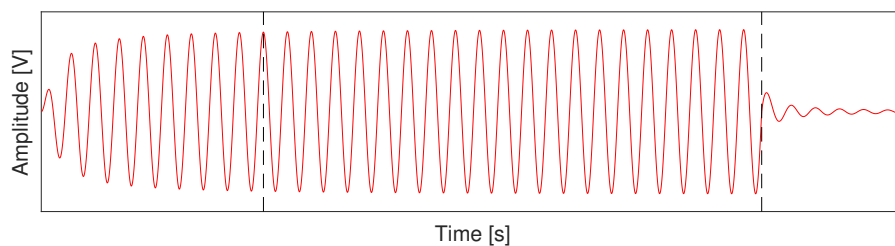
Figure 4-3: Time response of a monofrequency signal. The amplitude is constant between the two vertical dashed black lines.

Table 4-2: Input parameters for the stress-strain tests.

Input parameter	Value
Frequencies	200, 500 & 1000 Hz
Input amplitudes	10:10:100 mV
Signal time	0.5 s
Measurement time	0.6 s
Averages	50

4-4-2   Processing

The resulting force and acceleration time series at each frequency and amplitude are observed to find a section where the amplitude remains constant and the steady state regime has been reached. This excludes the data at the start of the time series where the amplitude is growing and the data at the end of the measurement where the signal has ceased (Fig. 4-3). In the time series data where the amplitude is constant, one period of data is extracted, where the time period, T, is the reciprocal of the input frequency (Fig. 4-4). From this one period, force and acceleration are converted to stress and strain using Equations (2-1) and (2-2), respectively, to produce stress-strain loops.
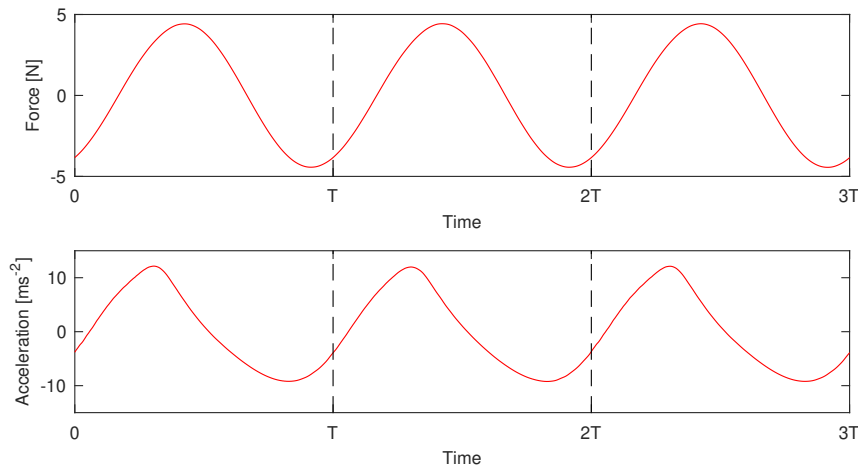
Figure 4-4: Force and acceleration time series from the gravel excited at 200 Hz. The x-axis is a function of the period of the input signal. One period is shown between one set of dashed black lines.

4-4-3   Results

The stress-strain loops for the gravel at excitation frequencies of 200, 500 and 1000 Hz at multiple frequencies are shown in Figure 4-5. All loops are established in a clockwise direction. The shape of the loops at 200 Hz are irregular where as the loops for 500 and 1000 Hz are shaped like ellipsoids. The maximum stress amplitude for these loops is approximately 2 kPa, as the input forces were the same across all frequencies. Whereas the strain amplitude, is different between the frequencies. The strain amplitude decreases with increasing driving

frequency from approximately 90 micro-strain at 200 Hz to 2 micro-strain at 1000 Hz. If the midpoint of the stress loops are taken (Fig. 4-5c), the midpoint of the 200 Hz loop would be a curve that flattens at high positive load. The midpoints of the 500 Hz and 1000 Hz loops would be approximately linear with a higher slope for the 1000 Hz loop as there is less strain for the same applied stress.

The dynamic stress cycles for the gravel at driving frequencies of 200, 500 and 100 Hz are compared to the steel spheres in Figure 4-6. The driving amplitude is 0.2 V in all cases. At 200 Hz, there is a large difference between the gravel and the steel spheres. The spheres have loops that are roughly equal whereas the gravel loop has a much larger area. At 500 and 1000 Hz, the opposite is true where the sphere loops are wider than the gravel. The spheres have a similar nature at 500 and 1000 Hz as their midpoint curves could both be approximated to be linear, with the midpoint slope steeper for the spheres at 500 Hz but the gravel has a steeper midpoint curve at 1000 Hz.

(a) 200 Hz.

(b) 500 Hz.
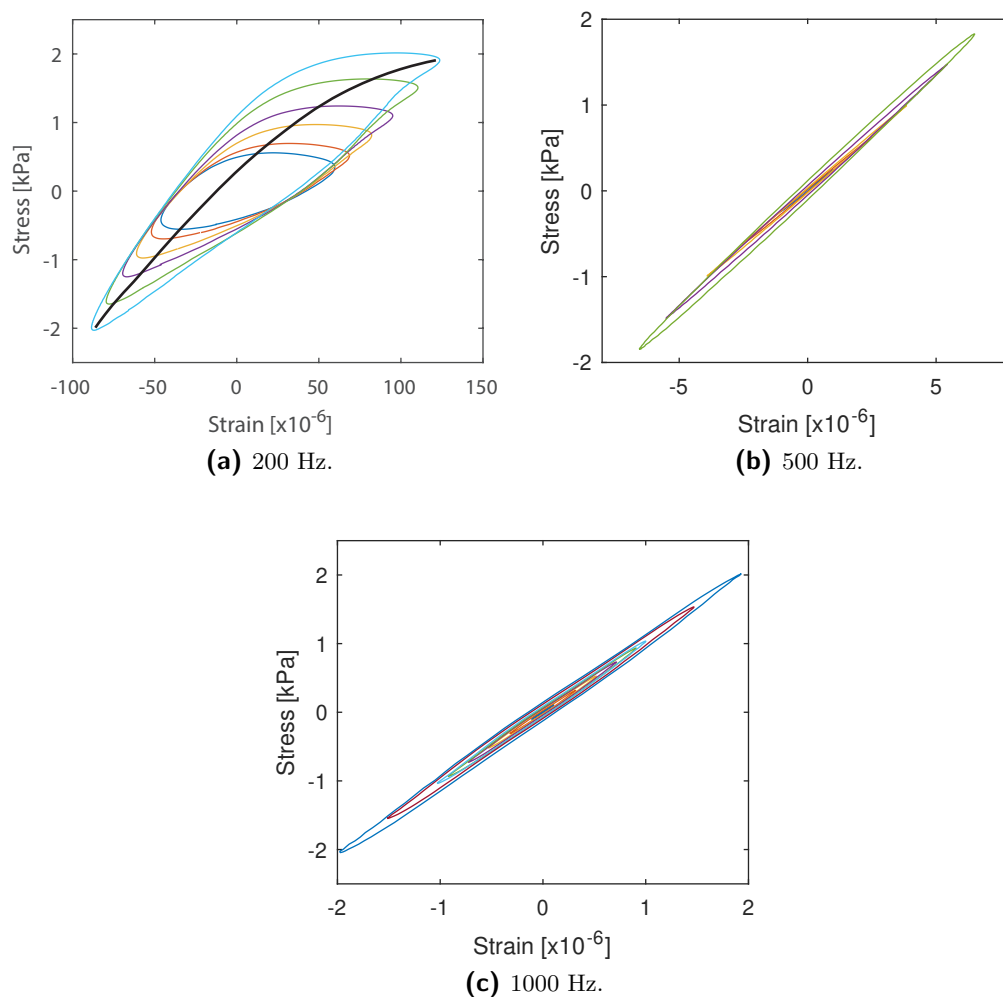
(c) 1000 Hz.

Figure 4-5: Stress-strain loops for the gravel at multiple amplitudes excited at 200, 500 and 1000 Hz. Black line on the 200 Hz plot denotes the mid point curve.

(a) 200 Hz.

(b) 500 Hz.
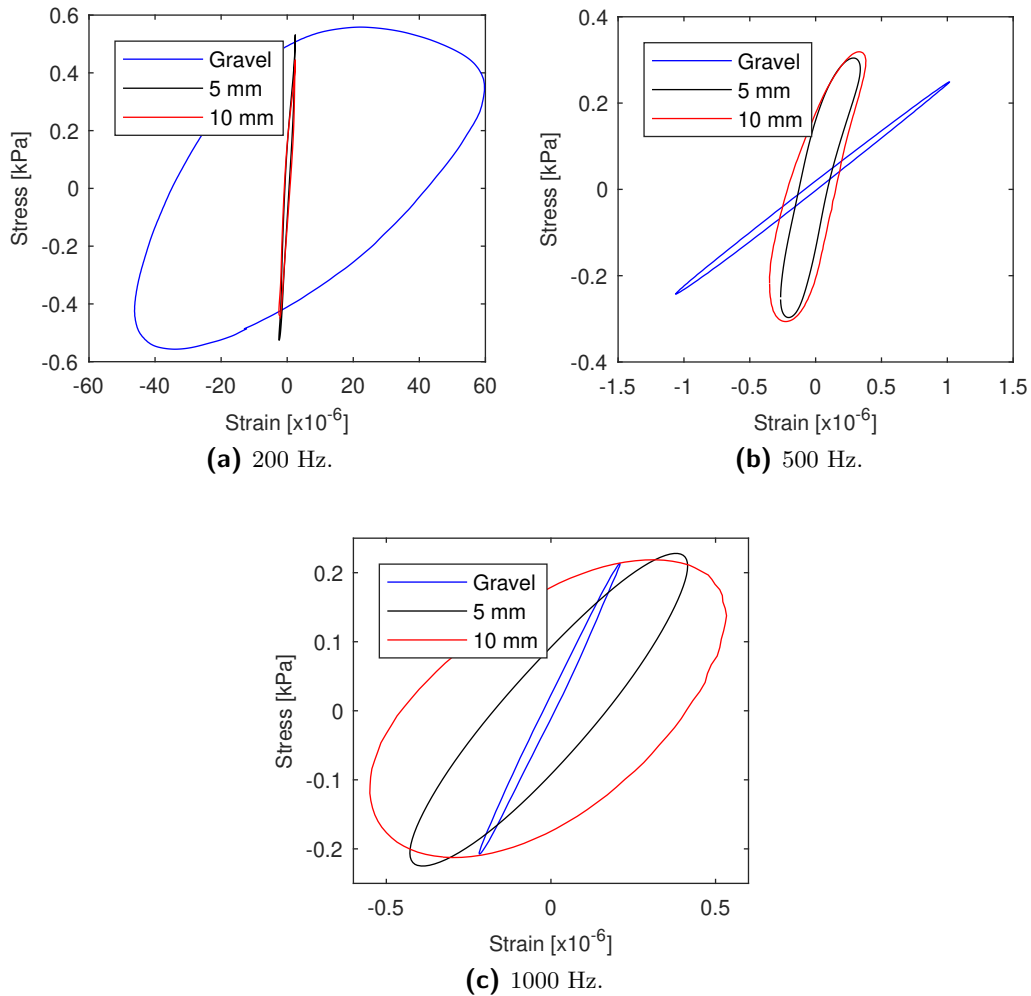
(c) 1000 Hz.

Figure 4-6: Force-displacement loops for the same input amplitude of 0.2 V for the three materials at 200, 500 and 1000 Hz.

4-4-4   Discussion

The non-regular shape of the gravel stress-strain loop at 200 Hz indicates that the nonlinearity is much stronger at this frequency. The midpoint curve of this loop flattens off at high positive load which shows strain softening. This means that the structure becomes weaker at higher load which is characteristic present in granular media. In addition, the midpoint curves become steeper with increasing driving amplitude, although this is less obvious at 500 and 1000 Hz. The midpoint curves are important as they are an approximation of the Young's modulus and as the midpoint slope increases with increasing driving force and increasing amplitude, both of these factors result in a higher value for the Young's modulus. Using the midpoint curves at a driving amplitude of 100 mV, the slope is approximately 22.6 MPa for 200 Hz, approximately 281 MPa for 500 Hz and approximately 1.02 GPa for 1000 Hz. This indicates that the excitation changes the rigidity of the material during the transient phase.

4-5 Resonance frequency shift

4-5-1 Acquisition

The resonance frequency is found experimentally by applying a frequency sweep to the material. The sweep consists of a sinusoidal waveform that varies in frequency over time (Fig. 4-7). The frequency change of the sweep depends on the frequency range and the sweep time. The frequency change can be linear or logarithmic. The measurement time is chosen to be slightly longer than the sweep time to allow for relaxation of the material, because the sweep is repeated and stacked to increase the signal-to-noise ratio. The input parameters are displayed in Table 4-3. The first sweep of the resonance tests takes the lowest amplitude, and subsequent sweeps will use successively higher amplitudes.
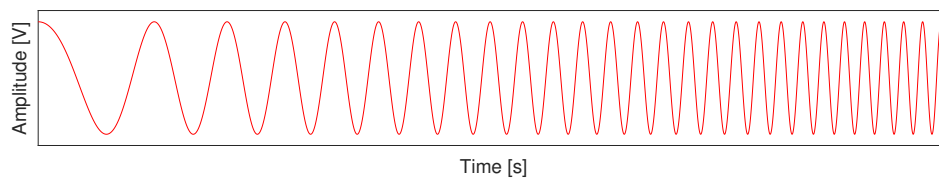
Figure 4-7: Time series of a sweep signal.

Table 4-3: Sweep input parameters for the resonance tests.

Input parameter	Value
Frequency range	50 - 1200 Hz
Frequency rate of change	Linear
Input amplitudes	10:10:100 mV
Sweep time	5 s
Measurement time	5.2 s
Averages	6

4-5-2 Processing

To retrieve the resonance peaks, the force and acceleration data are transformed to the frequency domain using a Fast Fourier Transform (FFT). The transfer function must now be calculated. A description of the transfer function will now be given.

The response of a medium in the frequency domain is given by

$$C(\omega) = H(\omega)U(\omega), \tag{4-1}$$

where C is the signal that arrives at a sensor after passing through the medium, U is the signal that is input into the medium and H is the transfer function. ω denotes the frequency domain. H can be obtained by spectral division

$$H(\omega) = \frac{C(\omega)}{U(\omega)}. \tag{4-2}$$

The calculation of the transfer function can be viewed as the ratio of the output, C, to the input, U.

For this experiment, the output is obtained by means of measuring the acceleration, $\ddot{x}$, and the input by measuring the Force, F. Thus, the calculation of the transfer function becomes

$$H(\omega) = \frac{\ddot{x}(\omega)}{F(\omega)}. \tag{4-3}$$

4-5-3 Results

Figure 4-8 shows the transfer function of the gravel. Several modes can be seen from applying the sweep. There are two modes with a relatively large frequency shift, at 240 Hz and 580 Hz. These two modes are boxed and labelled as resonance peak 1 and 2 respectively. There are also other clear modes at 310, 370 and 450 Hz where the frequency shift is much smaller. Higher order modes will exist but as the maximum sweep frequency was 800 Hz, they are not shown. As we are only interested in the first longitudinal mode (Fig. 2-10), only resonance peak 1 is considered. A close up of the resonance peaks of this mode are displayed in Figure 4-9a. It is clearly visible that as the driving force is increased, the resonance peak shifts to a lower frequency and the maximum value of the transfer function decreases. Figure 4-9b displays the normalised frequency shift plotted against the maximum force for the resonance curves in Figure 4-9a which shows a linear relationship. The peak frequencies of the resonance curves are used to obtain the Young's Modulus using Equation (2-21). The value of E for each peak is plotted against the maximum pressure, $P_{max} = F_{max}/A$ (Fig. 4-10). The y-axis intercept of the linear regression shows $E = 63.5$ MPa under zero pressure.
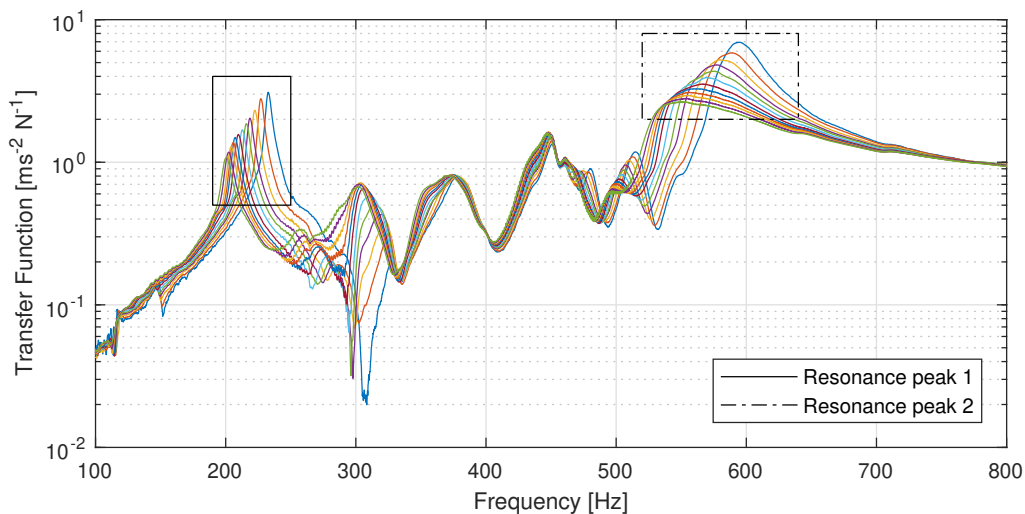
Figure 4-8: Transfer functions of the sweep for gravel, showing multiple resonance peaks. Frequency sweep was from 100 - 800 Hz.
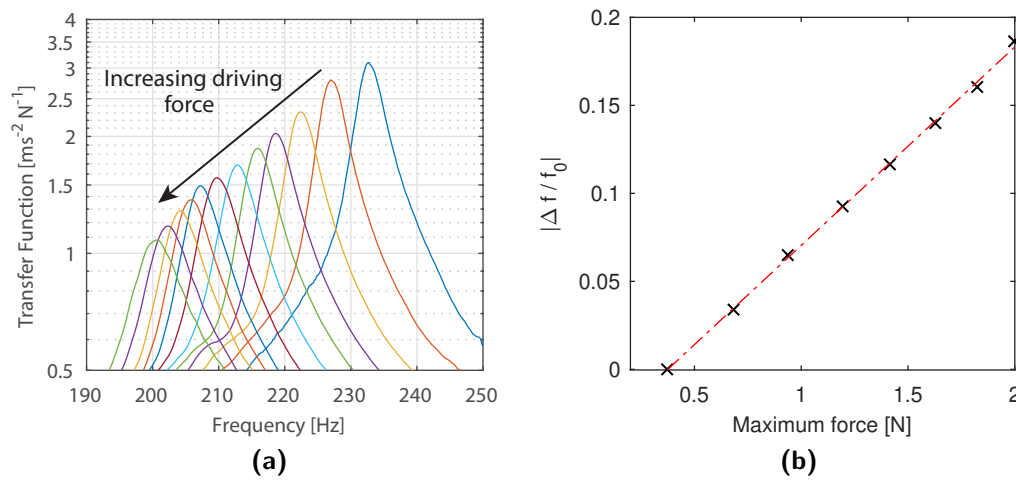
Figure 4-9: (a): Resonance curves for the first longitudinal mode of the gravel. (b): Normalised frequency shift against maximum force for the first longitudinal mode in gravel. The red dot-dashed line is a linear regression.
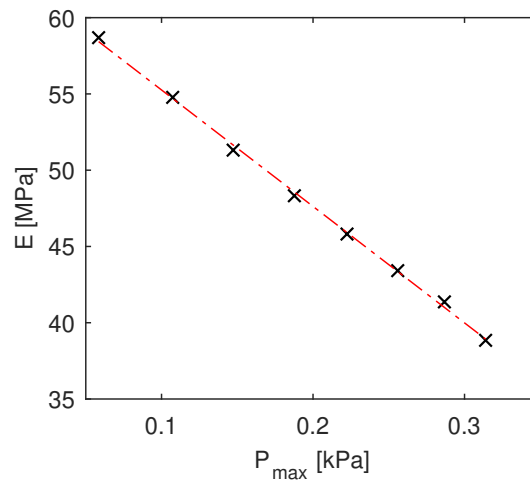
Figure 4-10: Young's Modulus, E, of the gravel against maximum pressure.

The same analysis for the resonance curves of the gravel is repeated for the steel spheres. The transfer function calculated from the sweep of the two sphere diameters is shown in Figure A-1. A close up of the resonance curves of the 1st longitudinal modes are shown in Figures 4-11a and 4-11b. The same trend of the resonance peak shifting to lower frequencies and a decrease in the transfer function with increasing driving force is observed for both steel spheres. The normalised frequency shift of the steel spheres shows a linear relationship with the maximum force (Fig. 4-11c & 4-11d). The Young's modulus is calculated for the steel spheres and displayed as a function of P_{max} (Fig. 4-11e & 4-11e). At $P=0$, the Young's modulus is 105.3 MPa and 114.3 MPa for the 5 and 10 mm diameter spheres respectively.
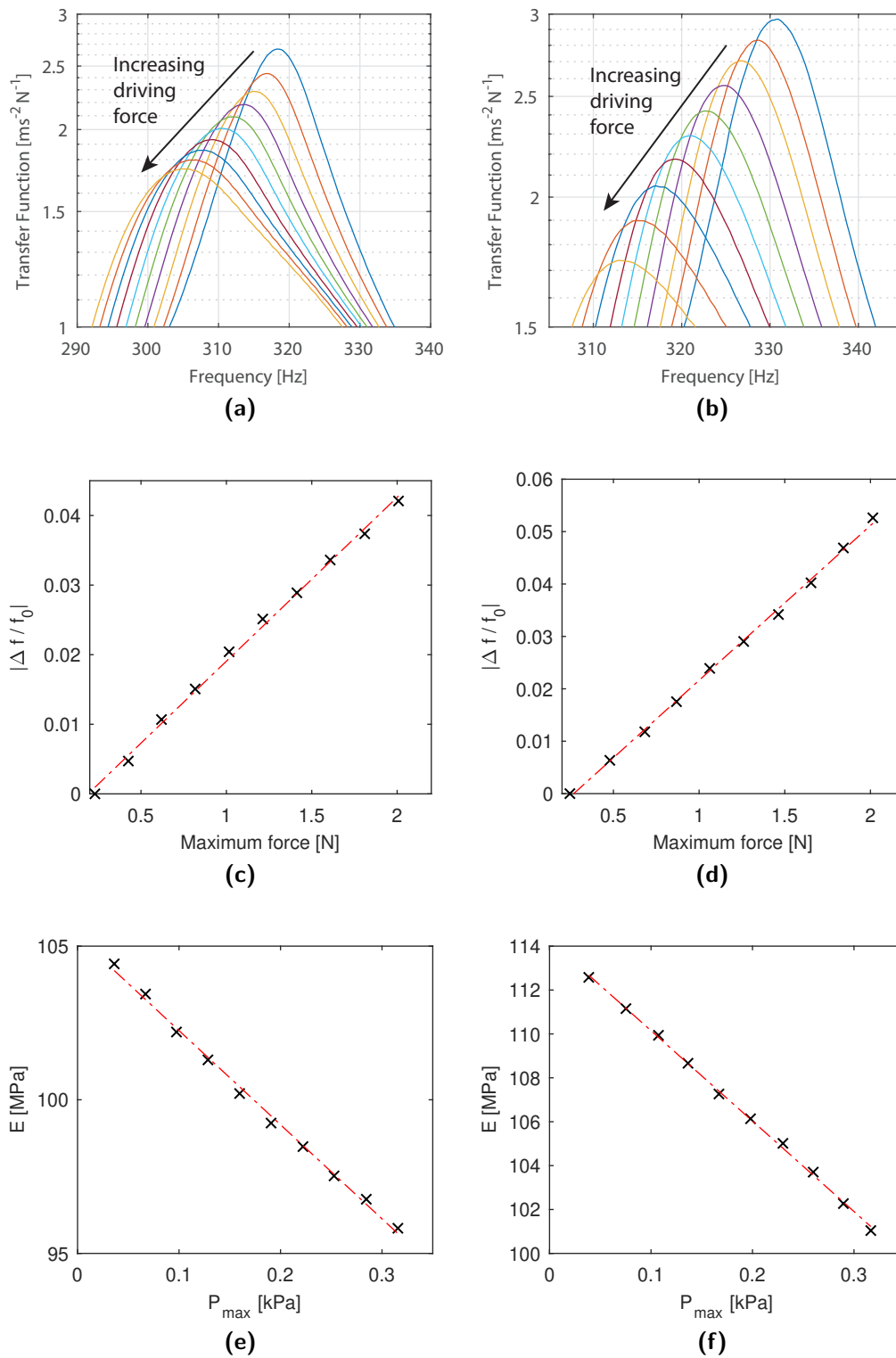
Figure 4-11: Transfer function of the first longitudinal mode for (a) 5 mm diameter and (b) 10 mm diameter steel spheres. Normalised frequency shift of the first longitudinal mode for (c) 5 mm diameter and (d) 10 mm diameter steel spheres. Young's modulus of the of the (e) 5 mm diameter and (f) 10 mm diameter steel spheres against maximum pressure.

4-5-4   Discussion

All three test materials produce a clear resonance shift for the 1st longitudinal mode. Other resonance modes are not required to calculate the Young's modulus. Analysis of this mode shows the same trends for all three materials with the resonance peaks shifting to lower frequencies and decreasing in amplitude for a higher driving force due to higher losses during transmission. All three materials exhibit a linear frequency shift with respect to the maximum force predicted by hysteretic nonlinearity. The Young's modulus is calculated at all of the driving amplitudes, so that when a linear regression is taken, the intercept can be calculated which is the value of E at zero pressure. For the gravel this is calculated to be 63.5 MPa, which is in the range of the Young's modulus for unconsolidated gravels of 30 - 320 MPa (Obrzud & Truty, 2012). The steel spheres Young's modulus at zero pressure is nearly double that of the gravel at 105 and 115 for the 5 mm and 10 mm diameters, respectively. The Young's modulus of bulk steel is approximately 100 GPa, therefore the homogenised Young's modulus of the steel spheres is 3 orders of magnitude lower than bulk steel.

4-6   Harmonic generation

4-6-1   Acquisition

Harmonics are generated in the material using the same excitation as the dynamic stress cycles (Fig. 4-3). The time period of the sinusoid depends on the required frequency and the number of periods. Initial testing found that having the number of periods equal to half the frequency in Hz produced a sufficient frequency plot, therefore the signal is applied for 0.5 s. Alike the resonance tests, the measurement time was set longer than the signal time to allow for relaxation between repeated measurements. The bursts are repeated at a constant frequency multiple time and stacked to improve the signal-to-noise ratio. The input frequency is then changed and the whole set of measurements at different amplitudes is run again. This process is repeated for various input frequencies. It can be noted that it is possible to measure the harmonics from the same data acquired for the dynamic stress cycles.

Table 4-4: Input parameters for the harmonic generation tests.

Input parameter	Value
Frequency	100, 200, 500 & 1000 Hz
Input amplitudes	10:10:200 mV
Signal time	0.5 s
Measurement time	0.6 s
Averages	50

4-6-2   Processing

The time response of the force and acceleration data are examined to find the time window where the data has reached the steady-state regime, thus a constant amplitude (Fig. 4-3). The head and tail of the response signals, during which the amplitude is changing, are ignored

in order to avoid transient effects in the data analysis. The accelerometer data in the chosen time window is transformed to the frequency domain using a FFT to obtain the harmonic peaks at multiples of the driving force frequency.

For analysis of the 2nd and 3rd harmonics, a plot of harmonic amplitude against strain amplitude is required. The harmonic amplitude of the 2nd and 3rd harmonic peaks is obtained from the FFT at double and triple the driving force frequency, respectively (Ostrovsky and Johnson, 2001). The strain amplitude is calculated using

$$\varepsilon = \frac{\ddot{x}}{\omega^2 L}, \tag{4-4}$$

where $\ddot{x}$ is the acceleration amplitude of the time response once it has reached the steady-state regime, ω is the angular frequency and L is the length of the sample. Note than this is only valid as it is assumed that the cylinder is behaving as a mass-spring oscillator.

4-6-3   Results

Figure 4-12 is an example of a frequency spectra showing the harmonics. Here, the gravel is excited at 500 Hz with a driving amplitude of 0.8 V and both odd and even harmonics are produced. The amplitude of the odd harmonics appears to be larger than the even harmonics.
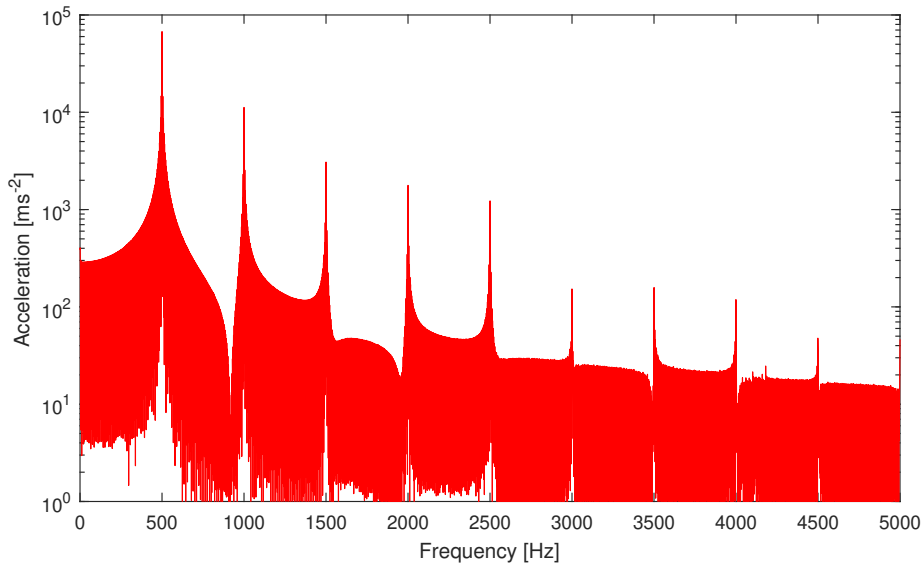
Figure 4-12: FFT of gravel excited at 500 Hz at a driving force of 0.8 V.

The gravel was excited at frequencies of 100, 200, 500 and 1000 Hz. The 2nd and 3rd harmonic amplitudes are plotted against the strain amplitude for each excitation frequency (Fig. 4-13). The excitation frequencies, give a range of strain amplitude from 10^{-7} to 10^{-4}. On a double logarithmic scale, the harmonic amplitude displays a linear relationship with the strain amplitude at all tested excitation frequencies. The slope for all plots is in the range of 1.1 - 1.3.
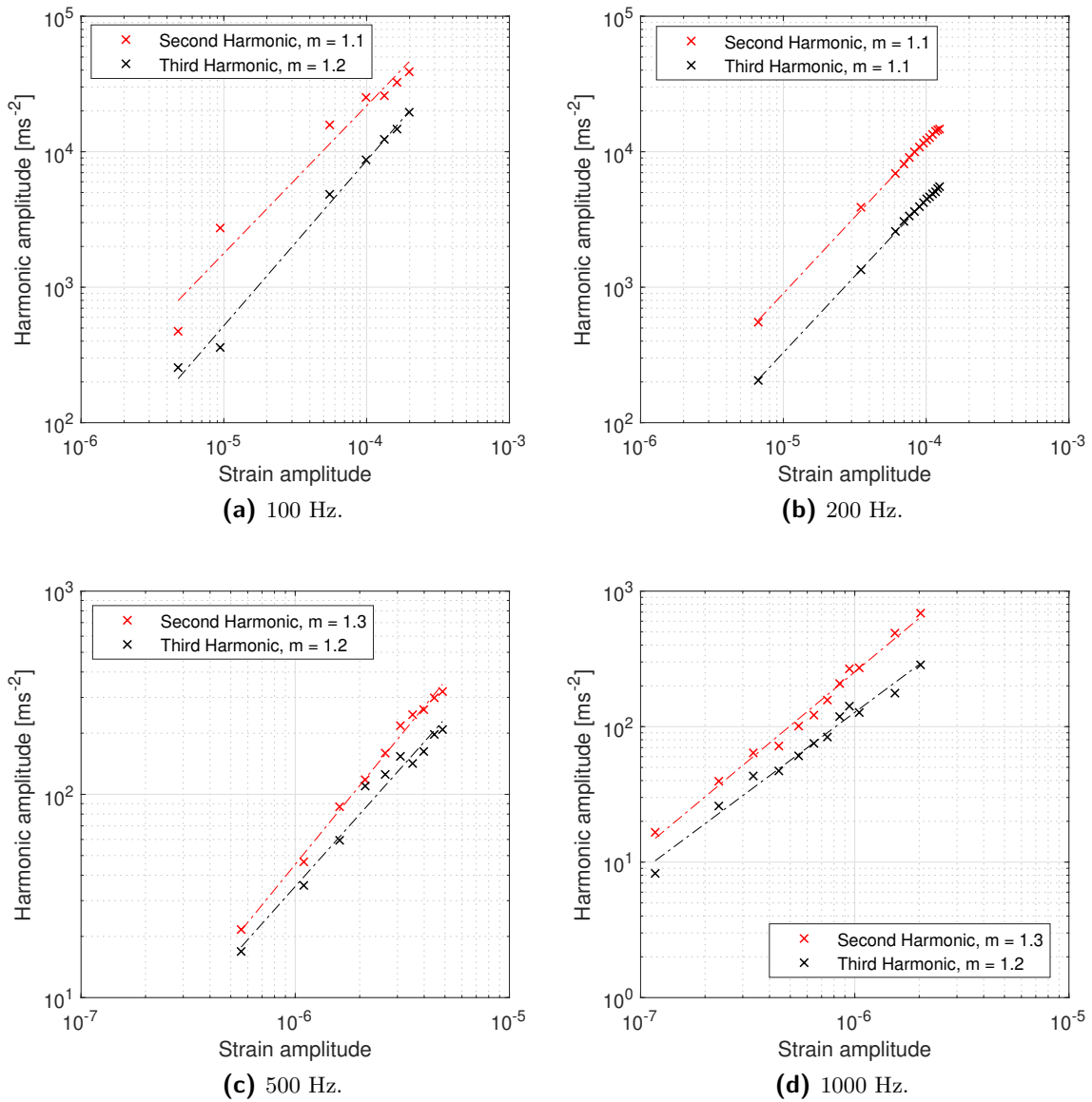
Figure 4-13: Strain amplitude dependency of the second and third harmonics for gravel.

The two sizes of steel spheres were excited at frequencies of 100, 200 and 1000 Hz. The 2nd and 3rd harmonic amplitudes are plotted against the strain amplitude for each excitation frequency in Figures 4-14 and 4-15 for the 5 and 10 mm diameter spheres, respectively. In logarithmic space, the harmonic amplitude displays a linear relationship with the strain amplitude at all of the tested excitation frequencies. The slope for all plots is in the range of 1.8 - 2.5.

(a) 100 Hz.

(b) 200 Hz.

(c) 1000 Hz.
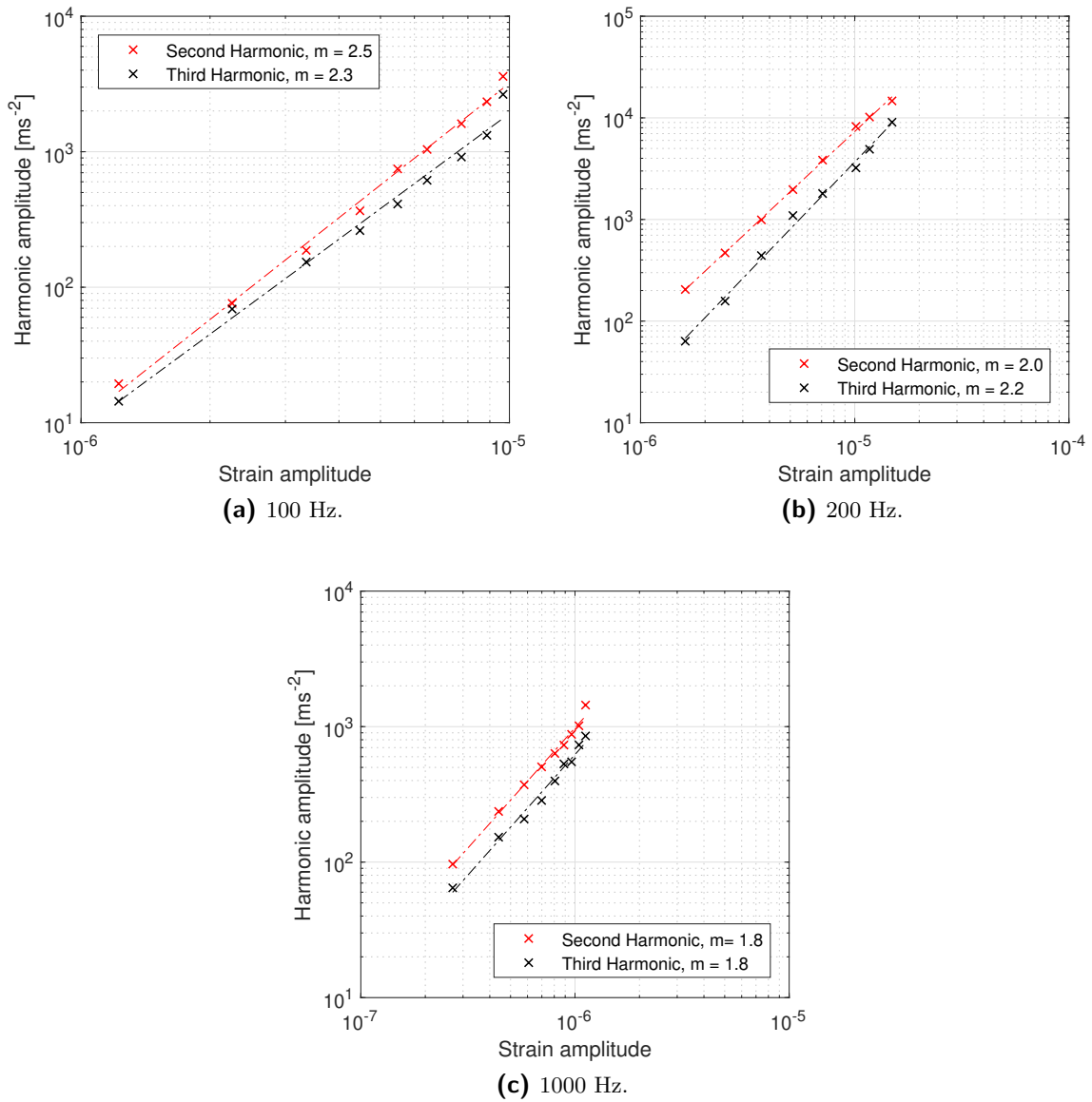
Figure 4-14: Strain amplitude dependency of the second and third harmonics for the 5 mm steel spheres.

(a) 100 Hz.

(b) 200 Hz.

(c) 1000 Hz.
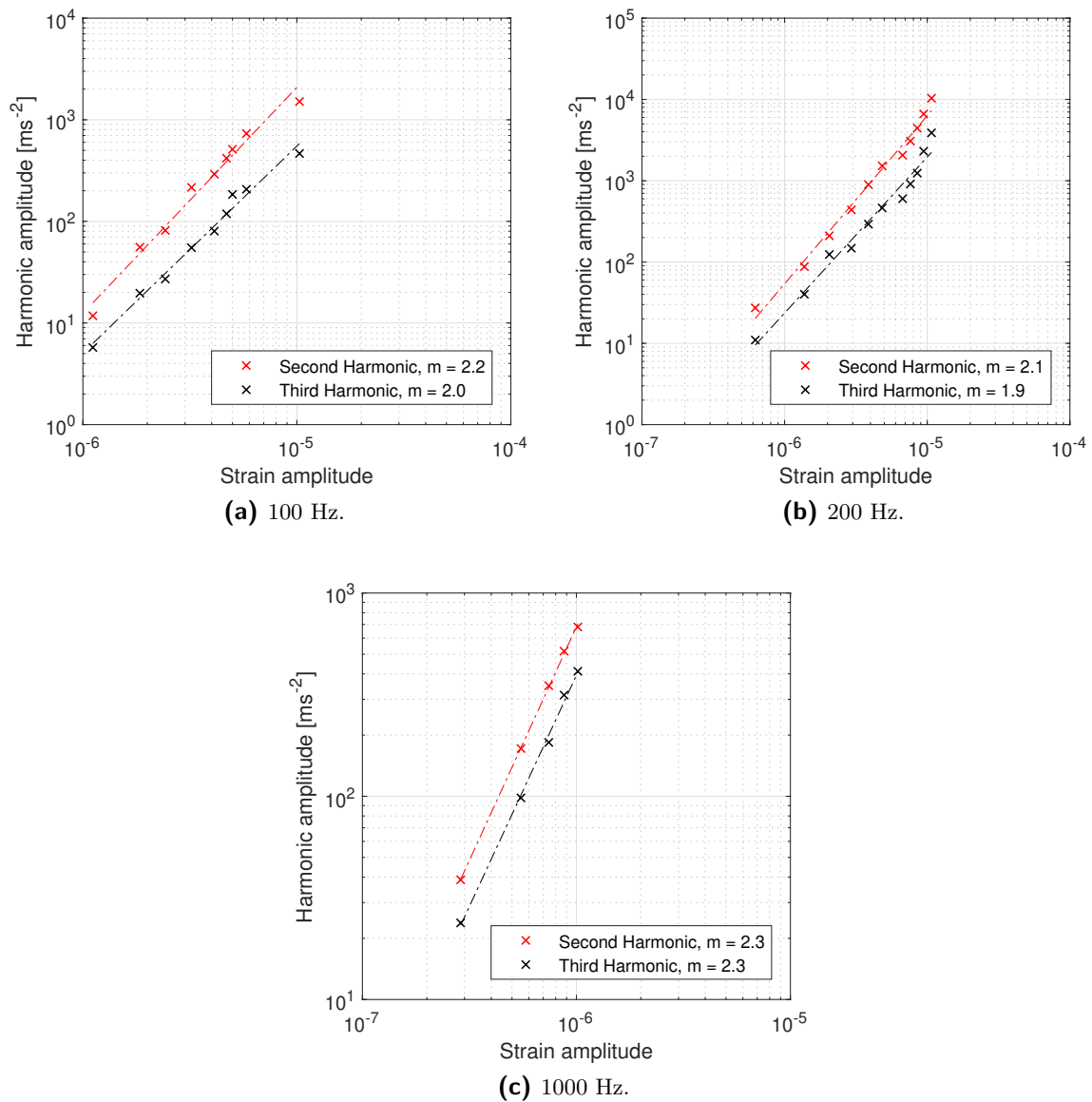
Figure 4-15: Strain amplitude dependency of the second and third harmonics for the 5 mm steel spheres.

4-6-4 Discussion

All harmonic slopes are consistent for the three materials in two ways, they are linear and the slopes of the 2nd and 3rd harmonics are sub-parallel. These results are no surprise as linear slopes in logarithmic space indicate nonlinear behaviour, whereas the slopes of the two harmonics being sub-parallel indicates that the nonlinearity is hysteretic and not classical (Van Den Abeele et al., 1997). The major difference between the gravel and the steel spheres is in the value of the slope. The gravel has a slope of just above 1 for each of the excitation frequencies, this can be approximated to a slope of 1, which means that there is a power

relation of 1 between the harmonic amplitude and the strain amplitude i.e., the relationship is approximately linear. The steel spheres display a slopes just above and below 2 for each of the excitation frequencies tested, this can be approximated to 2, which means that there is a power relation of 2 between the harmonic amplitude and strain amplitude i.e., the relationship is approximately quadratic. The value of the slope is used to calculate the nonlinear coefficients (Eq. (2-6)). Therefore, in the theoretical model the gravel will be described by different coefficients than the steel spheres.

4-7   Laser vibrometer

To provide a good comparison between the concept of linearity and nonlinearity, the vibrations of a free floating girder are directly compared with the vibrations of the same girder embedded in gravel. To achieve this, the girder is excited by a shaker using a frequency sweep and the vibrations of the girder are measured by a laser vibrometer. The laser vibrometer works by firing a laserbeam at the girder and measuring the beam as it is reflected back at the instrument. Due to the Doppler effect, when the oscillation of the vibrating girder is away from the vibrometer, the wavelength of the reflected beam will increase and and when the oscillation of the vibrating girder is towards the vibrometer, the wavelength of the reflected beam will decrease. The change in wavelength is detected as a phaseshift which allows the device to calculate the velocity of the vibrating girder.

The first part of this test involves exciting the girder as it is free floating. This is done by suspending the girder with cord from the ceiling (Fig. 4-16a). The shaker is mounted on a tripod and attached to the end of the girder where the shaker motion will be horizontal. A force sensor is attached between the girder and the shaker. The vibrometer must then be configured for the current measurement set-up. Firstly, the movement of the laserbeam is calibrated with the structure it is looking at and the laserbeam is autofocussed. A grid of points must be defined where each vibration reading will be taken across the surface of the girder. Retro-reflective tape is put on the girder where each measurement will take place to maximise the reflection of the laserbeam back to the instrument. Once the sweep input parameters are defined (Tab. 4-5), the program automatically applies a sweep to each measurement point while recording the force and velocity.

The same girder is then embedded in a 12 cm thick layer of gravel (Fig. 4-16b). The shaker is attached in the same location on the girder, but now the oscillations will be in the vertical direction. The girder is excited at 1 V for 5 minutes to allow for settling of the girder in the gravel. The configuration steps of the vibrometer described in the previous paragraph are repeated.
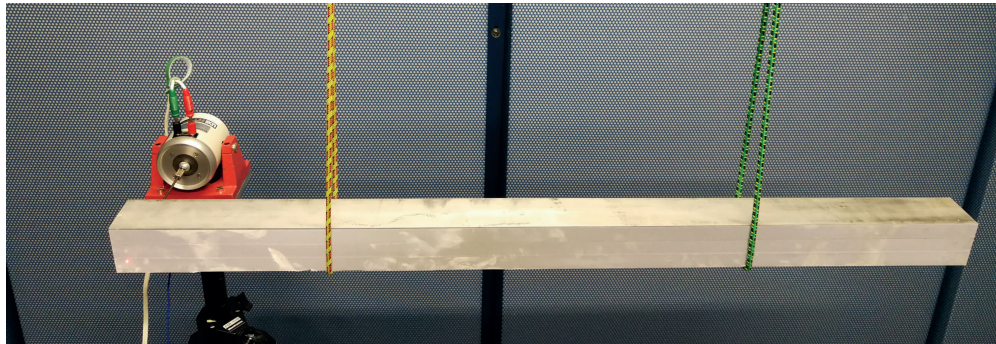
(a)

(b)

Figure 4-16: (a): Free floating girder. (b): Girder embedded in gravel.

Table 4-5: Input parameters for the laser vibrometer tests.

Input parameter	Value
Sweep	100 - 2500 Hz
Amplitude	50, 250 & 500 mV
Signal time	2.56 s
Measurement time	2.8 s
Averages	6
Measurement points	45

The transfer function is calculated for each point on the surface of the steel girder and the mean of all points is taken. The mean transfer function of the free floating girder is shown in Figure 4-17, where the two different sweep amplitudes are compared. Multiple peaks in the transfer function are clearly seen showing that multiple resonance modes are present. The difference in the transfer function between the two amplitudes is minimal. There is no shift in the peak frequency of the modes, there are only small differences at low transfer function amplitude due to noise.
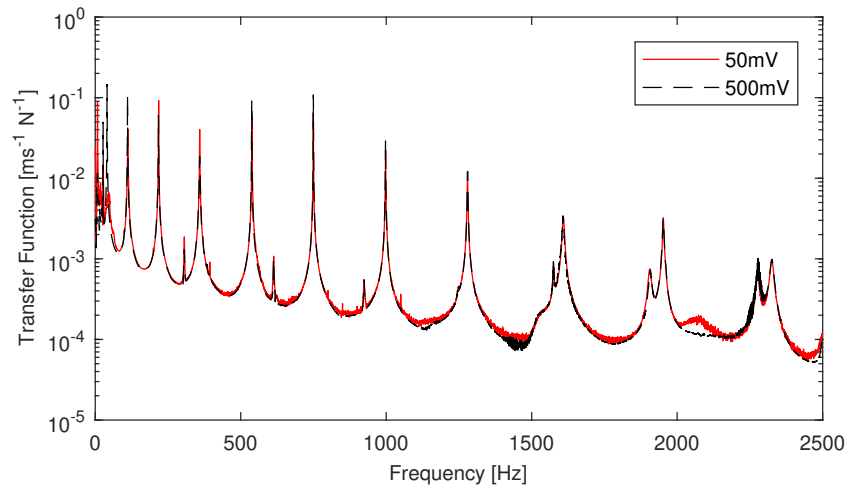
Figure 4-17: Transfer function between the velocity and force for the steel girder floating freely for input amplitudes of 50 and 500 mV.

For the girder embedded in gravel, the mean transfer function of all 45 points is taken and shown in Figure 4-18 where the two different sweep amplitudes are compared. Here, the effect of the gravel compared to the free floating girder is considerable. The peaks in the transfer function here are much less clear than for the free floating case and there are fewer of them. Another clear difference, is that the peak frequencies are different for the two sweep amplitudes used. The peaks of the higher amplitude sweep have shifted to the left. This shift is large for the peak at approximately 250 Hz at 50 mV, and smaller for peaks at approximately 1750 and 2250 Hz but still noticeable. In addition, not only has the frequency of the peaks shifted, but the peak amplitude has increased.
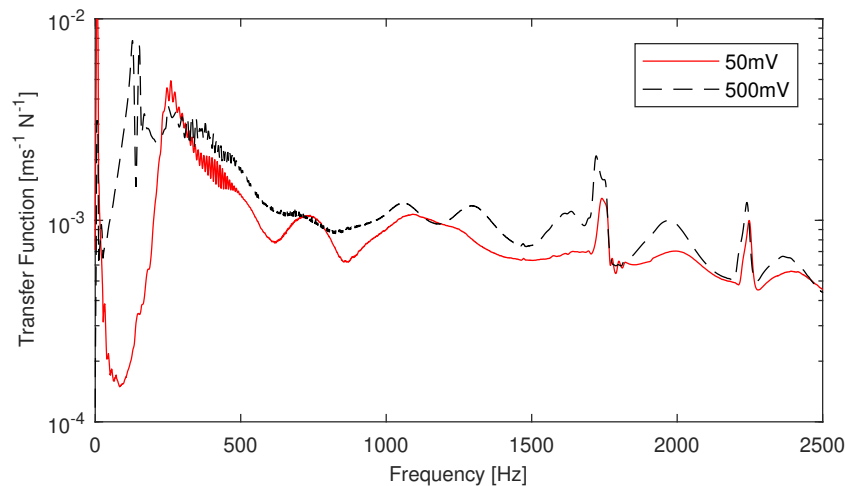
Figure 4-18: Transfer function between the velocity and force for the steel girder embedded in ballast for input amplitudes of 50 and 500 mV.

Chapter 5

Experimental study of wave transmission through unconsolidated granulates

5-1 Introduction

Granular media have a strong effect on the transmission of waves through its structure. Damping also plays a key role as movement of particles relative to each other leads to energy losses. The propagation of waves through unconsolidated granulates is investigated in this chapter, focussing on their transmissive and damping properties. Experiments will be carried out to investigate the effect of changing the thickness of the granular material, the effect of particle size and the relation between damping and the transfer function. These tests will figure out the effects of changing the thickness of material and particle size. This chapter will describe the apparatus used in the transmission experiments and give a description of each test procedure. After each procedure, the results are presented along with a discussion.

5-2 Apparatus and procedure

The transmission test consists of two set-ups. The first set-up is the same as the set-up used for the dynamic experiments (see Section 4-3) but in this case, the cylinder is placed directly on the floor. A more powerful shaker is used in comparison to the contained dynamic test. Due to its large weight and size, it is supported from above by a strap attached to a hydraulic crane. The stinger is then attached to the shaker and carefully screwed into the force sensor so that no force is being exerted on the mass by the weight of the shaker above. An additional accelerometer is used which is attached to the floor 30 cm away from the base of the cylinder.

The material is not contained in the cylinder for the second set-up but is piled onto the floor. Only gravel is used here as the steel spheres will not form a stable pile. The gravel is poured

onto the floor to cover a 1 x 1 m area and the top surface is levelled to make it flat. The mass used here is a 20 x 20 x 3 cm steel block with a mass of 7.482 kg and is placed centrally on top of the gravel pile. A force sensor is screwed into the top side of the mass where the shaker and stinger attaches. The same shaker is used for both set-ups. An accelerometer is attached to the top side of the mass using bees wax. Two additional accelerometers are attached to the floor adjacent to the gravel. The force sensor and accelerometers are connected to the same NI signal box, and all measurements are controlled using LabView software. Two additional accelerometers are mounted to the floor, 30 cm away from the edge of the gravel pile (Fig. 5-1).

Figure 5-1: Apparatus for transmission tests.

5-3 Acquisition

The transmission characteristics of the materials are determined by applying a frequency sweep (Fig. 4-7) with the aim of calculating the transfer function between the accelerometer on the floor and the accelerometer on the mass. The sweep applied has the same nature as shown in Figure 4-7. The parameters for these tests are shown in Table 5-1. The sweep is applied to both set-ups. The effect of the thickness on the transfer function is also tested here. The thickness of the gravel pile is changed to 100, 150 and 200 mm and the experiment repeated.

Table 5-1: Input parameters for the transmission sweep tests.

Input parameter	Value
Sweep	100 - 2500 Hz
Amplitude	0.05, 0.10 & 0.20 V
Signal time	5.0 s
Measurement time	5.2 s
Averages	10
Thickness	100, 150, & 200 mm

5-4 Changing thickness

The transfer function between the accelerometer on top of the mass and the floor accelerometer for each thickness of the gravel pile is shown in Figure 5-2. This transfer function contains many peaks at low frequencies ($\leq$500 Hz) and then it stays at roughly the same magnitude before there is a roll off. The frequency of this roll off, the cut-off frequency, is the same for each thickness. However, the slope of the roll is steeper for a thicker unit of gravel. At high frequencies ($\geq$1500 Hz), the transfer function of the 150 and 200 mm thick units are approximately equal, whereas the 100 mm thick unit has a higher amplitude.
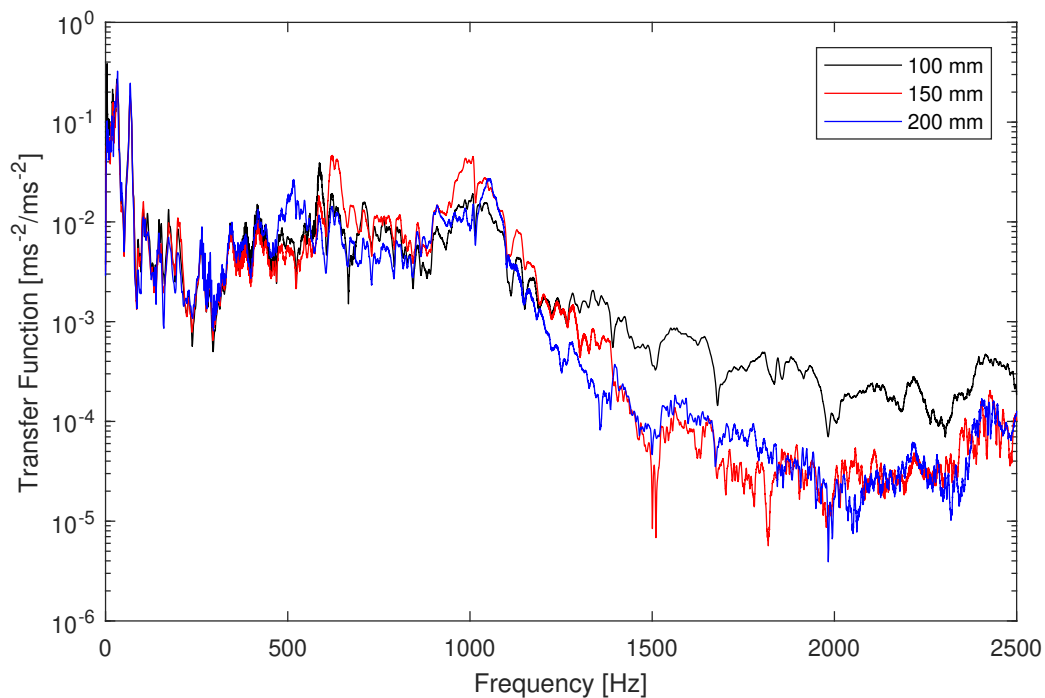
Figure 5-2: Transfer function between the accelerometer on the mass and the accelerometer on the floor for each thickness of the gravel pile.

5-5   Link between transfer function and damping

By comparing different transfer functions, the relative damping can be determined qualitatively. A lower transfer function indicates a higher level of damping in the material. If we compare the transfer function of the three test materials, for the same thickness of 11 cm inside the steel cylinder and input amplitude of 0.2 V, we get Figure 5-3. The input frequencies of 500 and 1000 Hz are considered. At 500 Hz, the transfer function is very similar for the two sizes of steel spheres, but is lower for the gravel. Therefore, the amount of damping in the 5 mm and 10 mm diameter steel spheres are similar but the damping in the gravel is higher. At 1000 Hz, the steel spheres now have different values for the transfer function. The 5 mm spheres have a larger transfer function than the 10 mm spheres which have a larger transfer function than the gravel. Thus, it can be deduced that the gravel has the highest amount of damping at this frequency, followed by the 10 mm spheres. With the least amount of damping in the 5 mm spheres.
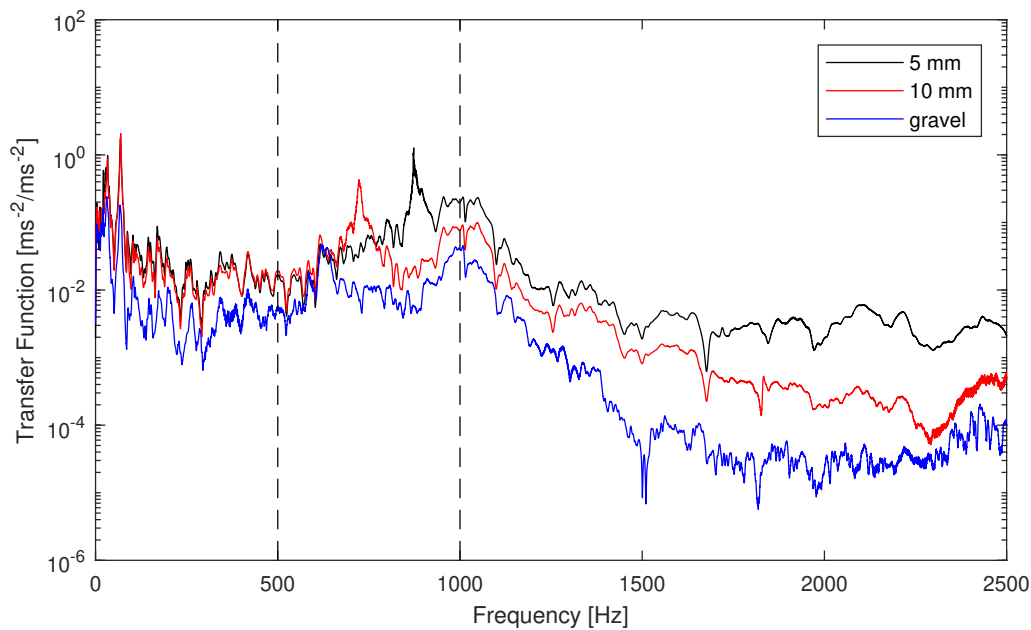
Figure 5-3: Transfer function of the three unconsolidated granulates for a constant thickness.

As explained in Chapter 2, the amount of hysteretic damping can be determined quantitatively by calculating the area of the hysteretic loop in force-displacement space. The force-displacement loops are shown in Figures 5-4a and 5-4b for input frequencies of 500 Hz and 1000 Hz respectively. These loops were measured at a constant input amplitude of 0.2 V with the same thicknesses of 10 cm. The area of all loops is shown in Table 5-2 which is equal to the energy loss per cycle. At 500 Hz, the loops of the steel spheres have a similar shape and the gravel loop is much narrower. The area of the 10 mm sphere loop is 50 % higher than the smaller steel sphere loop whereas, the 10 mm spheres have an energy loss higher than the gravel by nearly an order of magnitude. At 1000 Hz, the difference in energy loss between the three materials is more obvious, reflecting the transmission losses being different at this

frequency. The 10 mm steel spheres have an energy loss over double that of the 5 mm spheres which themselves have an energy loss an order of magnitude higher than the gravel.

(a) 500 Hz.
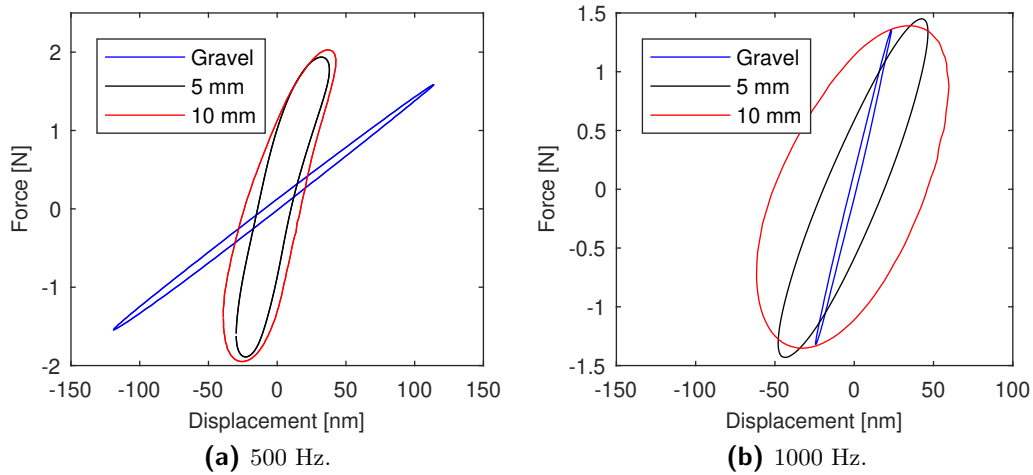
(b) 1000 Hz.

Figure 5-4: Force-displacement loops for the same input amplitude of 0.2 V for the three materials at 500 and 1000 Hz.

The transfer function in Figure 5-3 indicates that the amount of damping in the gravel is higher than that of the spheres. However, the hysteretic damping is much lower in the gravel than it is in the spheres. This is because there is additional inherent damping of the material which is not evident in the stress loops. Therefore, the inherent damping of the gravel must be much higher than that of the spheres to allow the total damping of the gravel to be much higher to see a lower value for the transfer function.

Table 5-2: Energy loss per cycle for the three test materials excited at 500 and 1000 Hz.

Frequency [Hz]	Gravel [J]	5 mm [J]	10 mm [J]
500	2.41×10^{-8}	8.87×10^{-8}	1.37×10^{-7}
1000	8.32×10^{-9}	8.72×10^{-8}	2.10×10^{-7}

Chapter 6

Finite Element Simulations

6-1 Introduction

Finite element modelling (FEM) is a general numerical technique to simulate a multitude of physical phenomena, ranging from thermal effects, static elasticity to wave propagation. FEM performs the simulation by approximating the solution of differential equations that describe the relevant physical process. The approximated solution is valid across the entire modelled structure, however complex in shape and nature.

FEM is a valuable tool for modelling the railway superstructure as multiple components can be defined. This is important here as the superstructure consists of the ballast, sleepers, rails and other features which FEM allows to be defined as separate components (Fig. 6-1a). The material properties of each component can be defined in addition to how the components are connected. The complex geometry of the superstructure is suited to FEM as meshing is used to accurately represent the true geometry (Fig. 6-1b). The mesh divides the structure into elements, with each element representing a set of algebraic equations defining the initial problem. All sets of element equations are combined into a global system of equations, which when solved reveals the total solution (Sayeed and Shahin, 2016). An example of this is shown in Fig. 6-1c, where the solution is the acoustic sound pressure level around the railway superstructure using the rail velocity as input. Once the model set-up is completed, the solution of all elements is available for analysis.
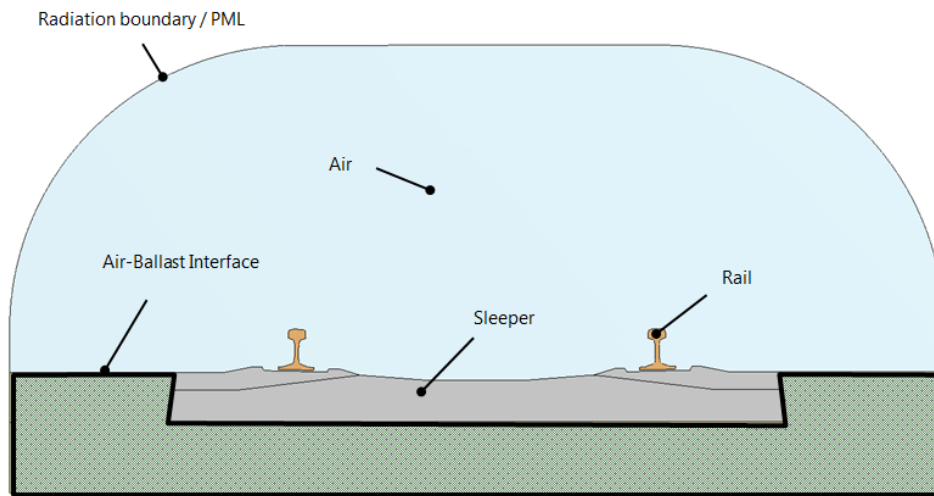
(a)
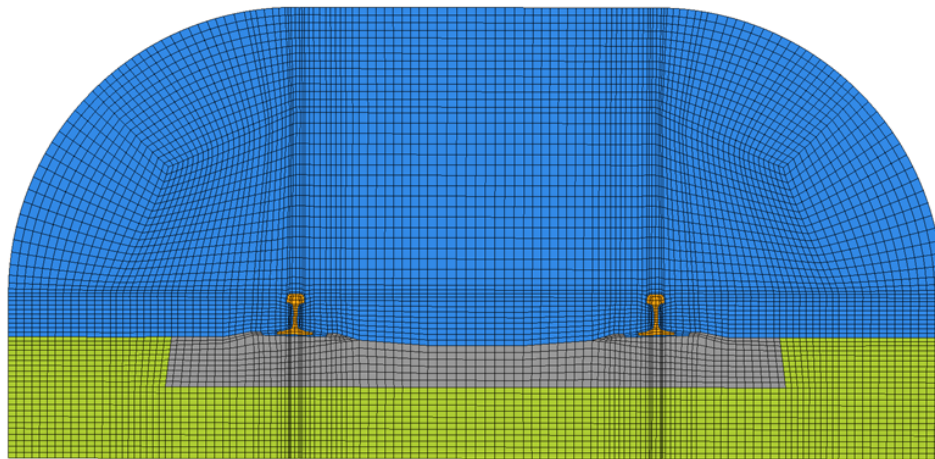
(b)
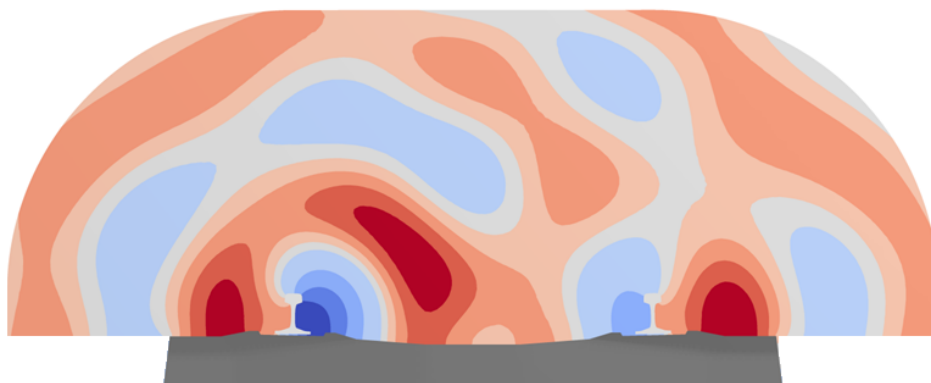
(c)

Figure 6-1: Cross-section through railway superstructure showing (a) the model components, (b) the mesh and (c) the total solution of the acoustic sound pressure level.

FEM is very convenient to simulate the dynamics of linear structures as modal analysis and frequency response functions can be computed rapidly, to determine what frequencies the structure will resonate at, and produce a spectrum of these frequencies. It also predicts the vibration amplitude under a general harmonic force load. However, this is not possible for nonlinear structures as their behaviour is amplitude dependent. To analyse nonlinear structures, the modal superposition technique is no longer valid. Therefore, the structural response has to be calculated for each and every excitation signal and amplitude, which is more time consuming but necessary to capture the nonlinear response.

In this chapter, the FEM technique is used to recreate the nonlinear behaviour of railway ballast using the experimental results described in the previous chapters. The chosen method is an adaptation of the spring-slider configuration used by Iwan (1966). Multiple spring-slider elements are used but with the addition of linear springs in parallel. The spring-slider elements are attached to a block with only displacement permitted in the axial direction of the springs, mimicking the experimental set-up shown in Figure 4-2. The model will be implemented to simulate the quasi-static and dynamic stress cycles. Using this numerical set-up, a parametric study of nonlinear resonance shift and harmonic generation is performed.

This chapter will give an overview of the modelling steps including creating the model, assigning model parameters and running the simulations. A discussion of how closely the model represents the experimental data is included as well as a comparison with previous hysteretic models.

6-2   Finite element implementation of a hysteretic support

6-2-1   Workflow

The software used to create the model and simulate experiments is ANSYS Workbench 18.2. This is an environment where all steps of the analyses are combined to perform the following workflow:

- Define engineering data
- Create geometry
- Set up model: assign material and mesh the geometry
- Define analysis settings: transient inputs and solver settings
- Run structural solver
- Post-processing: visualising results and exporting

6-2-2   Define engineering data

The engineering data are the bulk material properties for all required materials. The minimum properties required to define a material are the density and two elastic moduli, Young's modulus and Poisson ratio in this case. The density is set to 7850 $\mathrm{kgm^{-3}}$, although this is

arbitrary as the mass and inertia of the block are altered to the true values later. To negate the deformation of the block, so it acts rigid, the Young's modulus of the block is set to 20 TPa, 6 orders of magnitude higher than the gravel's Young's modulus of 60 MPa. A Poisson ratio of 0.3 is used.

6-2-3   Create geometry

The model geometry is created in a subpackage called DesignModeller. For this model, a 10 x 10 x 2 mm block is created, representing the mass placed on top of the unconsolidated granulates during the experiments (Fig. 6-2). A remote mass is coupled to all 6 faces of the block to bring the total mass up to the same as the cylindrical mass used in the experiments i.e., 1.482 kg.
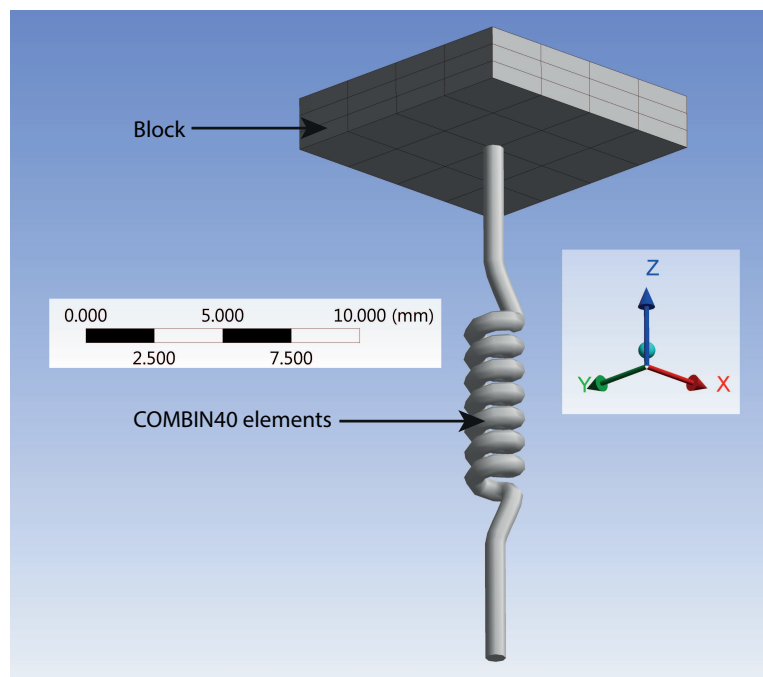
Figure 6-2: Spring and block model in ANSYS. The spring represents a set of 50 multiple spring-slider elements in parallel, all acting in one point of the mass.

6-2-4   Set up model

Boundary conditions of the model must be defined to limit the degrees of freedom. A frictionless support is applied to the 4 edge faces of the block parallel to the axial direction of the spring-slider elements. This means that the block can only move along the z-axis, in accordance with the main motion of the mass in the experiment. The base of the springs is fixed.

Meshing of the block is required. This discretises the domain into a 3D mesh required by the FE solver. For meshing, the MultiZone method is used. This method automatically decomposes the geometry into a pure hexahedral mesh. The element order is linear.

As it is not possible to input hysteretic properties into a homogeneous material, spring-slider elements are used to represent the granular support of the rigid mass. The elements used in this model are defined as connections and coupled to the central node on the base of the block (Fig. 6-2). The element *COMBIN40*, a nonlinear spring which is available in the software library, is used here and many of these elements can be created in parallel. Each COMBIN40 element consists of a spring-slider with spring constant k^Y and yield force f^S, a linear spring with spring constant k^{NY}, a damper with damping coefficient C and a gap functionality (Fig. 6-3). These parameters have to be defined for each spring, and will define the agreement between the model and experimental results. The elements are set to have only one degree of freedom of movement, in the axial direction of the springs.
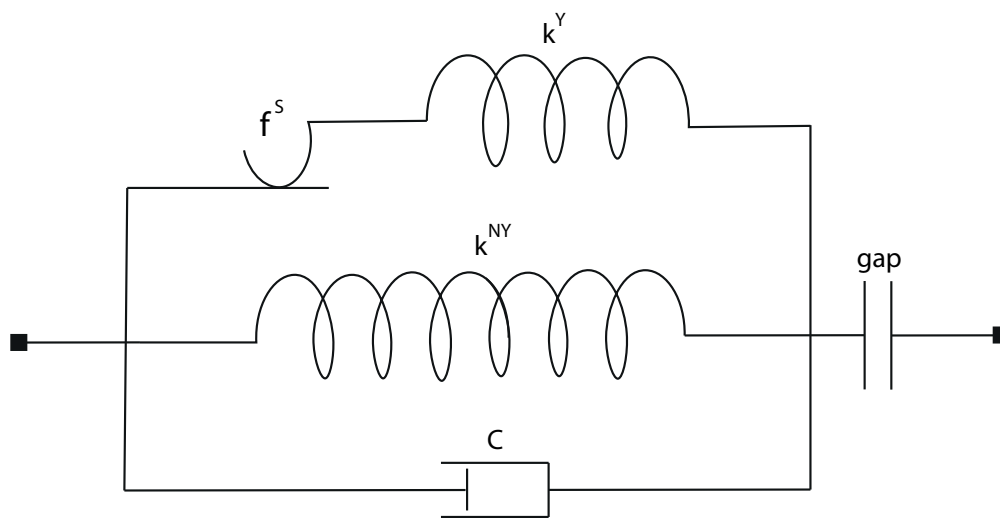
Figure 6-3: COMBIN40 element consisting of a spring-slider with spring constant k^Y and yield force f^S, linear spring with spring constant k^{NY}, a damper with damping coefficient C and a gap functionality.

When a displacement is applied to a single COMBIN40 element, assuming the gap is closed, the initial force-displacement curve has a slope of the sum of the spring constant of the non-yielding spring, k_{NY}, and the spring constant of the yielding spring, k_Y. When the force in the spring-slider reaches f^S, the slider activates and the force in the yielding spring does not increase further. The force-displacement curve now has a slope of k_{NY}. When the displacement direction reverses, the force-displacement curve will have have a slope of $k_{NY} + k_Y$ as both springs relax. The slider will activate again at $-f^S$ and the $f - x$ curve will have a slope of k_{NY}. This differs from the behaviour of single spring-slider as shown in Figure 2-8. The addition of the non-yielding spring in the COMBIN40 element allows the maximum force to be infinite whereas the total force is bounded by f^S for the single spring-slider.

If the gap in the COMBIN40 element is activated and the total force across the element becomes zero, the force in both springs is set to zero. If further displacement occurs to open the element, the gap will open to allow for this. This means that the total force across the element cannot be negative which is the case in the quasi-static tests. The COMBIN40 element relates to the stick-slip motion at granular contacts without having to model each contact.

6-2-5 Define analysis settings

The analysis settings are defined to produce suitable results for the simulations. For the quasi-static tests, static structural analysis is used where the displacement is defined as the input, as was the case for the experiment. For the dynamic tests, transient structural analysis is used where the the force is applied as the input. The time-step is set to 2.5×10^{-4} for a 200 Hz input signal, 1×10^{-4} s for a 500 Hz input signal and 5×10^{-5} s for a 1000 Hz input signal. Additional settings, refering to the solver parameters, are set to *program controlled* apart from the solver type which is set to *iterative* as convergence of the solution at each time-step is required. The input displacement and force are applied to the very top face of the block and act in the axial direction of the springs.

6-2-6 Run structural solver

The simulation is meaningless unless output quantities are defined. The relevant output quantities for these simulations are force and displacement. For the quasi-static tests, the output is the force. This is retrieved from the force reaction in the spring elements. For the dynamic tests, the required output is the time response of displacement. The displacement is retrieved from the total displacement of the block in the axial direction of the spring elements.

6-2-7 Post-processing

Post-processing includes plotting of the output quantities. A force-displacement graph is created within the program to instantly show the results in a meaningful way once a simulation is complete.

6-3 Retrieving the model parameters

6-3-1 MATLAB model

To retrieve a set of spring parameters, an analytical model of the COMBIN40 elements is created in MATLAB for the quasi-static and dynamic cases. Such a script rapidly computes the model solution under the simplified mass-spring assumption. This means that tens of parameter tests can be made in the same time as running one test in the FE solver. As the railway superstructure is modelled using FEM, the final simulations of the ballast will also be computed by FEM and not with the analytical model. Doing this, more complicated effects can be modelled, such as the deformation of the rails and sleepers, the acoustic radiation, and the wave propagation towards the environment.

A MATLAB script was created to analytically simulate the FE model. The results showed that using 50 COMBIN40 elements in parallel was an optimum number as adding more elements made the results negligibly more accurate, thus 50 springs was deemed computationally efficient.

6-3-2 Quasi-static analytical model

Firstly, the parameters for the 50 COMBIN40 elements have to be defined. In theory, 250 parameters can be chosen freely, 5 for each spring element. Since an optimisation of this scale falls outside the scope of the project, simplified relations were chosen for sets of unknown parameters. The spring constants for both the yielding and non-yielding springs are given a linear distribution across the 50 elements, the yield forces and gaps are given a logarithmic distribution across all 50 elements. The damping coefficient is set to zero for all elements, as damping is not applicable to static cases.

Additional restrictions on the free parameters can be derived by analysing a single experimental stress loop (Fig. 6-4). The sum of all spring constants, k_{tot}, is the slope when the load direction is reversed after maximum force has been applied. The sum of all non-yielding spring constants, k_{tot}^{NY}, is also known as it can be picked from the experimental data as the approximate slope before maximum positive load is applied, after all yielding springs have yielded. For the quasi-static tests with activated gap, the smallest gap, g_1, is the value of the displacement when the force begins to increase.
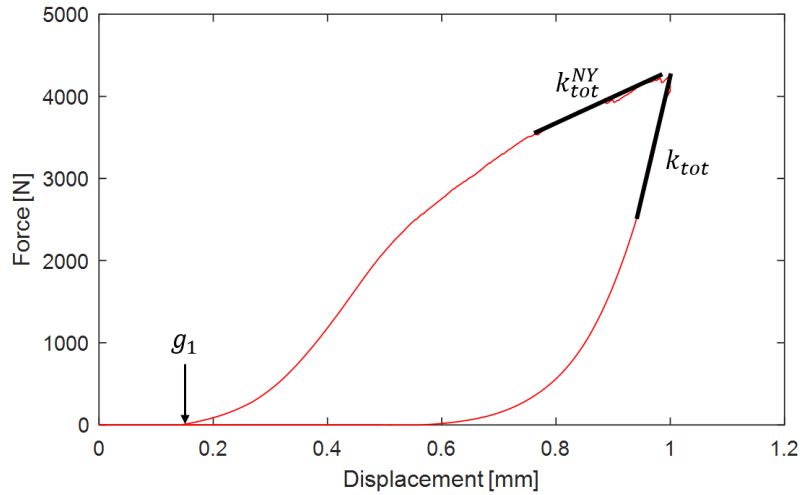
Figure 6-4: Model parameter restrictions extracted from quasi-static stress loop.

The sum of all spring constants is the sum of all non-yielding spring constants, k_{tot}^{NY}, plus the sum of all yielding spring constants, k_{tot}^{Y}

$$k_{tot} = \sum_{i=1}^{N} k_i^{NY} + \sum_{i=1}^{N} k_i^{Y} = k_{tot}^{NY} + k_{tot}^{Y}. \tag{6-1}$$

Therefore, k_{tot}^{Y} is also known as it is just the difference between these two

$$k_{tot}^{Y} = k_{tot} - k_{tot}^{NY}. \tag{6-2}$$

The linear distribution of non-yielding springs has a separation of Δk^{NY}, this results in the arithmetic series

$$k_{tot}^{NY} = [k_1^{NY} + (k_1^{NY} + \Delta k^{NY}) + (k_1^{NY} + 2\Delta k^{NY}) + ... + (k_1^{NY} + (N-1)\Delta k^{NY})], \quad (6\text{-}3)$$

where k_1^{NY} is the spring constant of the first non-yielding spring. The result is

$$k_{tot}^{NY} = \frac{N(2k_1^{NY} + (N-1)\Delta k^{NY})}{2}. \quad (6\text{-}4)$$

The separation can be calculated by rearranging this equation

$$\Delta k^{NY} = \frac{2(k_{tot}^{NY} - Nk_1^{NY})}{N(N-1)}. \quad (6\text{-}5)$$

Analogously, the linear distribution of yielding springs has a separation of Δk^Y resulting in the arithmetic series

$$k_{tot}^Y = [k_1^Y + (k_1^Y + \Delta k^Y) + (k_1^Y + 2\Delta k^Y) + ... + (k_1^Y + (N-1)\Delta k^Y)], \quad (6\text{-}6)$$

where k_1^Y is the spring constant of the first yielding spring. The result is

$$k_{tot}^Y = \frac{N(2k_1^Y + (N-1)\Delta k^Y)}{2}. \quad (6\text{-}7)$$

The separation for the distribution of yielding springs can be calculated by rearranging this equation and substituting in Equation (6-2)

$$\Delta k^Y = \frac{2(k_{tot} - k_{tot}^{NY} - Nk_1^Y)}{N(N-1)}. \quad (6\text{-}8)$$

The yield force is given a logarithmic distribution between two unknowns, f_a^S and f_b^S. The logarithmic distribution for the gaps are bounded by g_1 and g_N, where the latter is unknown. Therefore, the quasi-static case has 5 unknowns to fit to the experimental data: k_1^{NY}, k_1^Y, f_a^S, f_a^S and g_N.

As 5 degrees of freedom would be too time consuming to fit by hand, a genetic algorithm script in MATLAB is used to find the best fitting parameters. This works by first setting upper and lower limits for each parameter to fit. The algorithm then randomly generates a value for each parameter between the defined limits. This is done multiple times to create multiple parameters sets called the *population*. Initial tests found that a population of 60 produced consistent results while being computationally efficient, so the size of the population was set to this value. The force-displacement response is then calculated using the analytical MATLAB script for the whole population (Fig. 6-6a). Each time the models are calculated for the population is called a *generation*. The input is the displacement measured during the experiment. The sum of the square error (SSE) between the model output and experimental data are calculated for each member of the population (Fig. 6-5). For the quasi-static case, the error is calculated from the output force and the experimental force. The population is

then sorted in order of increasing SSE. The population with 10 % of the lowest SSE are kept for the next generation and the 30 % with the highest SSE are discarded. The remaining 60 % are grouped into pairs and a random value is taken between the model parameters for each pair, for the next generation. The final 30 % of the next generation population is created randomly in the same method as the first generation. This is done so that optimised parameters do not fall into a local minimum. The model is then calculated again for the population of the next generation and the process is repeated. As the generations progress, the population gets a more improved fit to the experimental results (Fig. 6-6b), until it converges. Convergence was typically reached after 60 generations.
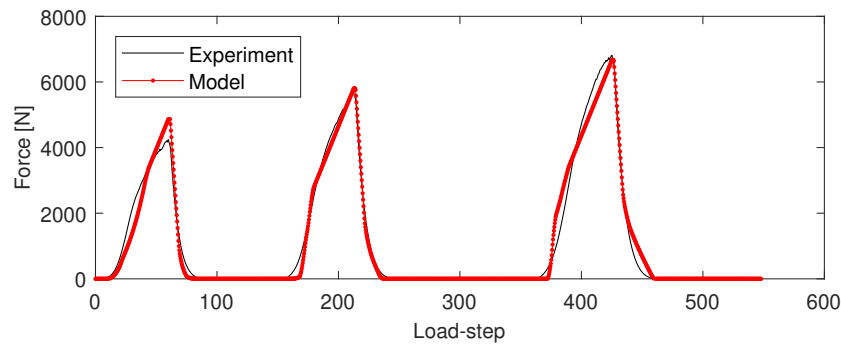
Figure 6-5: Experimental and model output values for force response to static displacement. The SSE is calculated from these values.

(a) 1st generation.   (b) 25th generation.
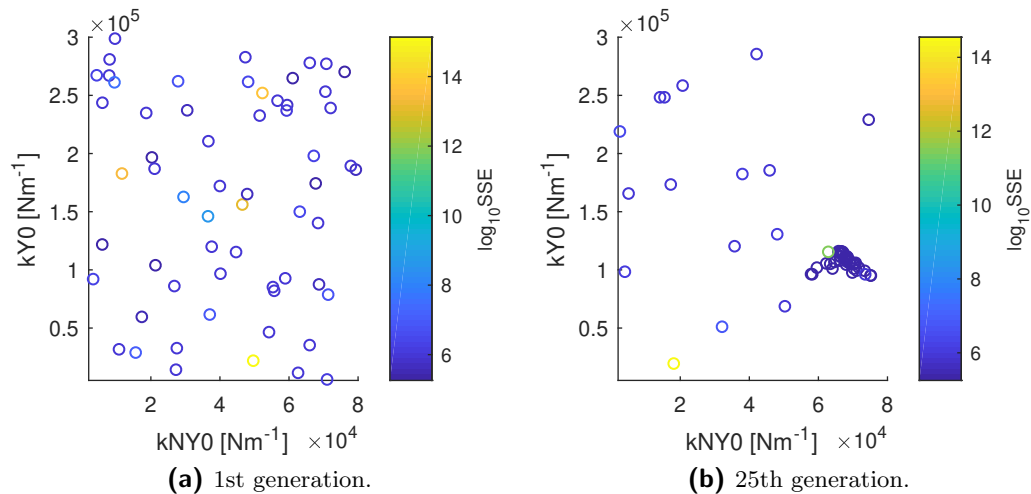
Figure 6-6: Values of two model parameters after the 1st and 25th generation of the genetic algorithm. Parameters are clearly converging in the latter.

In Section 3-3, multiple stress cycles were applied at increasing amplitudes. A simulation of the same conditions were performed using the analytical model (Fig. 6-7). The optimised model parameters for this result are shown in Table 6-1. These define the distribution for the spring constants, yield forces and gaps.
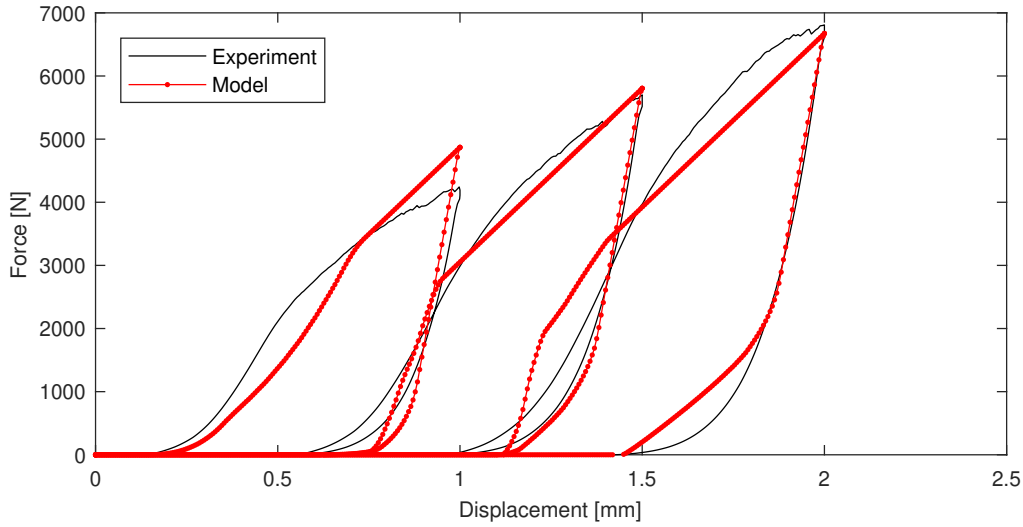
Figure 6-7: Analytical MATLAB model of the quasi-static stress cycles using model parameters from the genetic algorithm.

Table 6-1: Model parameters for the quasi-static simulation.

Model parameter	Value
k_{tot}	30.5×10^6 Nm^{-1}
k_{tot}^{NY}	4.9×10^6 Nm^{-1}
g_1	0.143 mm
k_1^{NY}	1.42×10^4 Nm^{-1}
k_1^{Y}	9.27×10^4 Nm^{-1}
f_a^S	26.75 N
f_b^S	58.88 N
g_N	0.673 mm

6-3-3   Dynamic analytical model

Due to the orders-of-magnitude difference in driving forces between the quasi-static and dynamic case, the previously retrieved spring parameters do not provide sufficient fitting for the dynamic problem. Therefore, new model parameters are required. This means that a dynamic analytical model is required for transient analysis. This is more complex than the quasi-static case as the following equation has to be solved

$$m\frac{d^2x}{dt^2} + C\frac{dx}{dt} + \sum f = F, \tag{6-9}$$

where m is the mass, C is the damping coefficient, $\sum f$ is the sum of all spring forces and F is the input force. To solve this equation, it is discretised using a finite difference approximation. The central scheme is used for the second order derivative and a backward scheme is used on the first order derivative

$$m \left(\frac{x^{t+1} - 2x^t + x^{t-1}}{\Delta t^2} \right) + C \frac{x^{t+1} - x^{t-1}}{2\Delta t} + \sum f^t = F^t, \tag{6-10}$$

where Δt is the time-step and x is the displacement at the time-step specified in the superscript. This equation can be rearranged to solve for x

$$x^{t+1} = \frac{4mx^t + x^{t-1}(C\Delta t - 2m) + 2\Delta t^2 (F^t - \sum f^t)}{2m + C\Delta t}. \tag{6-11}$$

The sum of the all forces in the spring elements are calculated by a separate MATLAB function for each time-step. As a first approach, for fitting purposes only, the gaps are not activated in the calculation. The sum of square errors is calculated for the time response of the displacement as the time response of the model force is obtained from the experimental data. The distribution of spring constants and yield forces of the 50 elements are calculated in exactly the same way as in the quasi-static case. However, in the dynamic case, the damping coefficient is now non-zero. As no gaps are present, this removes g_N from the unknowns but the damping coefficient is added as an unknown, C. The total spring constant, k_{tot}, is retrieved from the midpoint curve of the 500 Hz stress cycle at an amplitude of 0.2 V (Fig. 6-8a). The midpoint curve is approximated to be linear. To simplify the model even more, the total spring constant of the non-yielding springs, k_{tot}^{NY}, is assigned a value where the ratio of k_{tot}^{NY}/k_{tot} is the same as the quasi-static case.

The genetic algorithm was used again to fit the 5 unknowns to the results of the MATLAB model. The error is calculated from the displacement time response of the models and experiments. The model parameters produced by the genetic algorithm are shown in Table 6-2 along with the parameters obtained from the experimental data. The optimal model parameters produce the fit shown in Figure 6-8b.
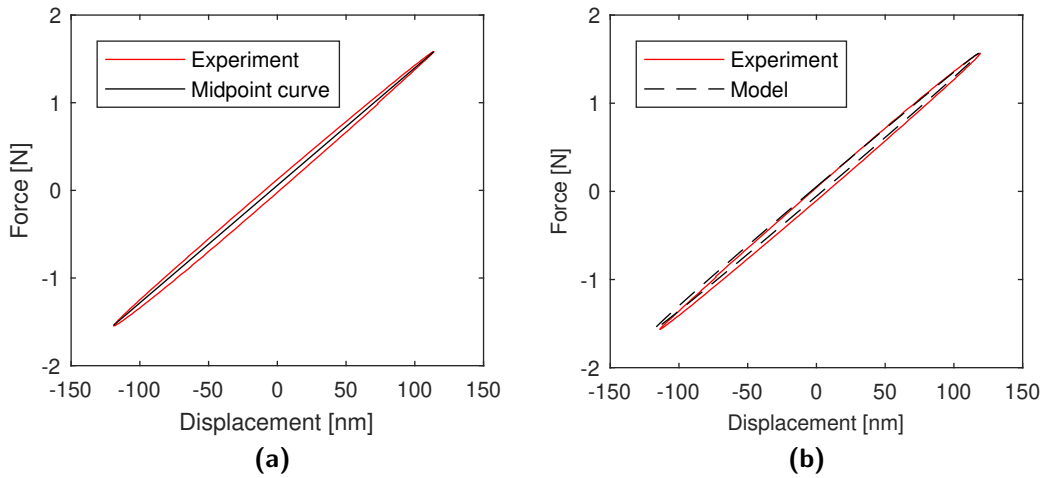
Figure 6-8: (a): Midpoint curve of the dynamic stress cycle at an input frequency of 500 Hz and input force of 1.584 N. (b): Analytical MATLAB model of a dynamic stress cycle at 500 Hz using model parameters from the genetic algorithm.

Table 6-2: Model parameters for the dynamic simulations with no gap functionality.

Model parameter	Value
k_{tot}	7.92×10^6 Nm^{-1}
k_{tot}^{NY}	1.22×10^6 Nm^{-1}
k_1^{NY}	1.41×10^4 Nm^{-1}
k_1^{Y}	2.13×10^5 Nm^{-1}
f_a^{S}	1.532×10^{-4}N
f_b^{S}	6.672×10^{-4} N
C	147.0 Nsm^{-1}

6-4 FEM results

6-4-1 Quasi-static simulation

The model parameters from the genetic algorithm for the quasi-static case are input into the FE model containing the spring-slider elements. This is done by calculating the parameters for each element and grouping the parameters for all elements in a table. The table is then imported into ANSYS to define the COMBIN40 elements.

In Section 3-3, multiple stress cycles were applied at increasing amplitudes. FE simulations of the same conditions were performed. The results of the quasi-static simulation are shown in Figure 6-9.
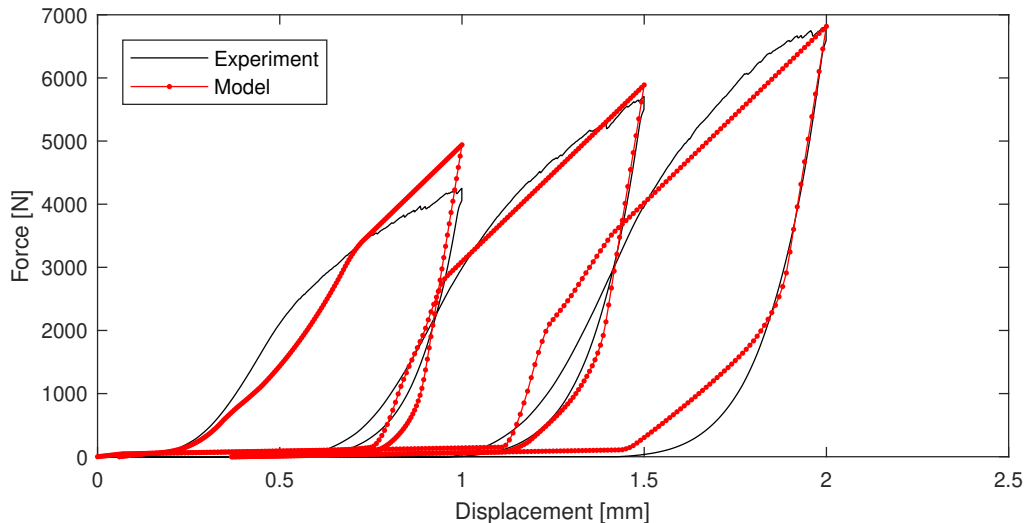
Figure 6-9: FEM result of quasi-static stress cycles using model parameters from the genetic algorithm.

The results of the FEM are comparable to the analytical MATLAB model, however there are small discrepancies at very low force. The fit of the FEM stress cycles to the experimental data is rather good. The maximum force in the first stress loop is too high but the other two

loops match well. The loading curves for each loop have the worst fit, especially as the latter part of the loading curve is linear in the model. However, the unloading curves are modelled very well and the plastic deformation, represented by the shift in each stress loop, is clearly exhibited by the model.

6-4-2   Dynamic simulations

Implementing parameters

The model parameters from the genetic algorithm for the dynamic case are input into the COMBIN40 elements in the FE model, as described in the same way as the quasi-static simulations. The results are first calculated for with the gap disabled. Then, the gaps are enabled in the elements without changing the model parameters. Initial testing found that the model was unstable with the gap activated for all 50 elements, therefore the gaps were only activated for the first 40 elements which produces stable results. The presence of the gaps changes the spring behaviour, and attempts to find quantitative agreement were as yet unsuccessful. The results shown aim to highlight the qualitative relations between the model and experimental data.

Dynamic stress cycles

The role of the damping coefficient and gaps are investigated for different input amplitudes and frequencies. In Section 4-4, the dynamic stress cycles of the gravel were obtained using a monofrequency excitation force. FE simulations of the same conditions were performed with the model parameters in Table 6-2. The model comparison to the experimental data at 500 Hz is shown in Figure 6-10. The model provides a good fit at an input force of 0.759 N (Fig. 6-10a), however, when the input force is increased to 6 N, the midpoint curve of the model data is less steep than the midpoint curve of the experimental data (Fig. 6-10b). The area of the two loops appears very similar which shows that the damping parameter is accurate.

The model comparison to the experimental data at 1000 Hz is shown in Figure 6-11a. When the driving frequency is 1000 Hz, the midpoint curve of the model and experimental data match. However, the model loop has a much smaller area than the experimental loop indicating that the damping parameter is mismatched, by manually changing only the parameter C, increasing C from 147 Nsm^{-1} to 750 Nsm^{-1} (Fig. 6-11b) yields the model to better fit the experimental data as the loop becomes larger without any change to the slope of the midpoint curve.

(a) 0.759 N.

(b) 6.312 N.
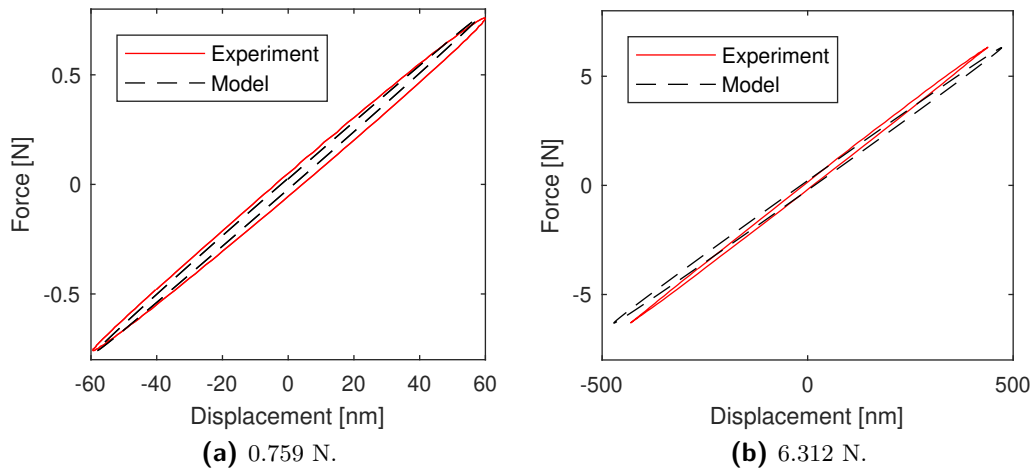
Figure 6-10: Dynamic stress cycle of 500 Hz at different driving forces.

(a) C = 147 Nsm^{-1}.

(b) C = 750 Nsm^{-1}.
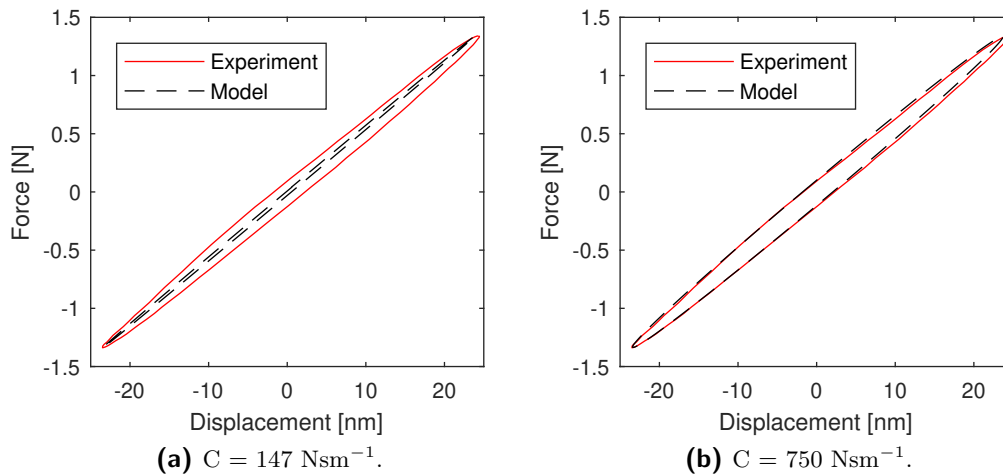
Figure 6-11: Dynamic stress cycle of 1000 Hz with different damping coefficients.

The first approach of the dynamic simulations described above deactivates all element gaps. A second approach enables the gap functionality of the elements and continues to use the model parameters from the first approach. The gap functionality is enabled for 40 out of the 50 elements. The simulations performed are repeated. The resulting model loops do not fit the experimental data, as the parameters have not been optimised for gap functionality. Nevertheless, the first approach always produces symmetric loops whereas the experimental stress loops at 200 Hz are asymmetric. The presence of gaps is able to produce asymmetric loops at 200 Hz (Fig. 6-12a). In addition, the FE model with gaps can produce models with figure-of-eight shaped loops (Fig. 6-12b). These appeared in the experimental results at low frequency excitations of 100 Hz.
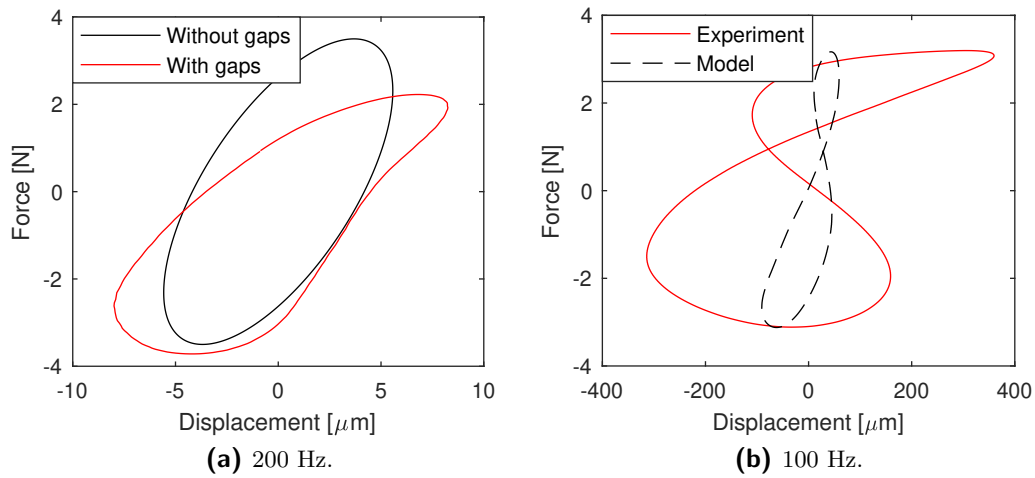
(a) 200 Hz.

(b) 100 Hz.

Figure 6-12: (a): Dynamic stress loops at 200 Hz produced with and without gaps. (b): Dynamic stress loops generated with gaps displaying a figure-of-eight loop at 100 Hz as experienced in the experimental data.

Harmonic generation

In Section 4-6, the presence of higher harmonics was measured at 200, 500 and 1000 Hz, at excitation forces varying from 0.05 to 2 N. The experimental conditions were replicated for the simulations to validate the FE model. For the approach without gaps, the FFT of the resulting displacement reveals that only odd harmonics are generated (Fig. 6-13a) indicating that the model is purely hysteretic and that there are no components that represent classical nonlinearity present. Analysis of the third harmonic reveals a linear slope for all three input frequencies, with a value approximating 1 (Fig. 6-14). This is the same slope that was found in the gravel by the experimental results (Fig. 4-13).

(a) Without gaps.

(b) With gaps.
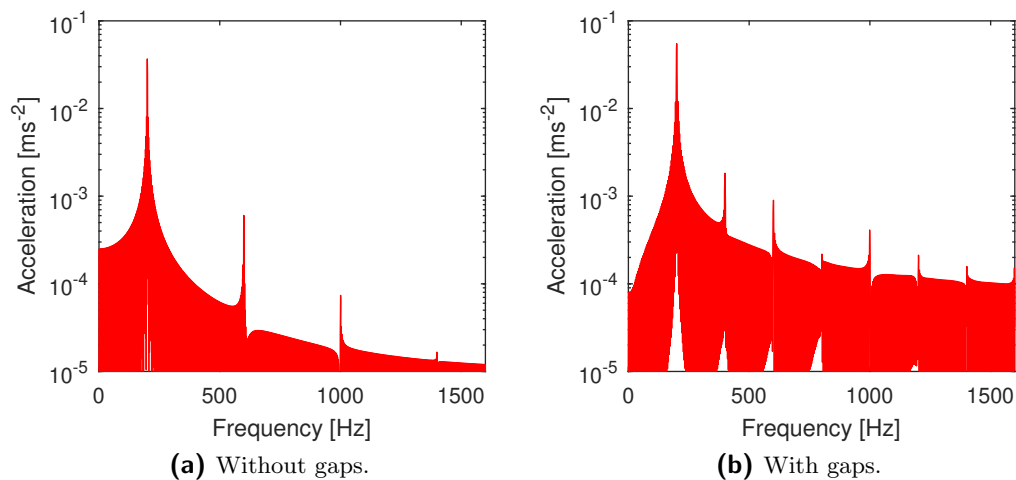
Figure 6-13: FFT of simulated data using FE elements with and without gap functionality.

When the gaps are enabled, the resulting FFT of the data shows that both odd and even harmonics are generated (Fig. 6-13b), as experienced in the experimental data. This indicates that the gaps must be providing a component of classical nonlinearity as they are not present in the first approach. Analysis of the second and third harmonic amplitude also shows a linear dependence on the strain amplitude with slopes of approximately 1 for all frequencies (Fig. 6-15), matching the experimental results.
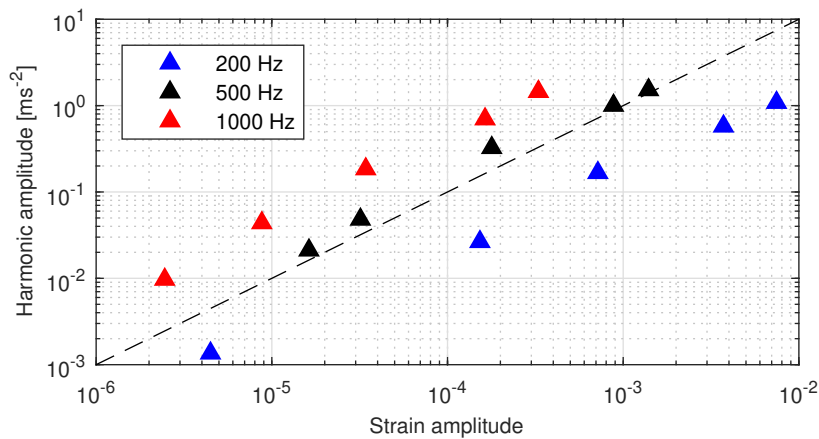
Figure 6-14: Third harmonics of the dynamic simulation without gaps. The dashed line denotes a slope of 1.
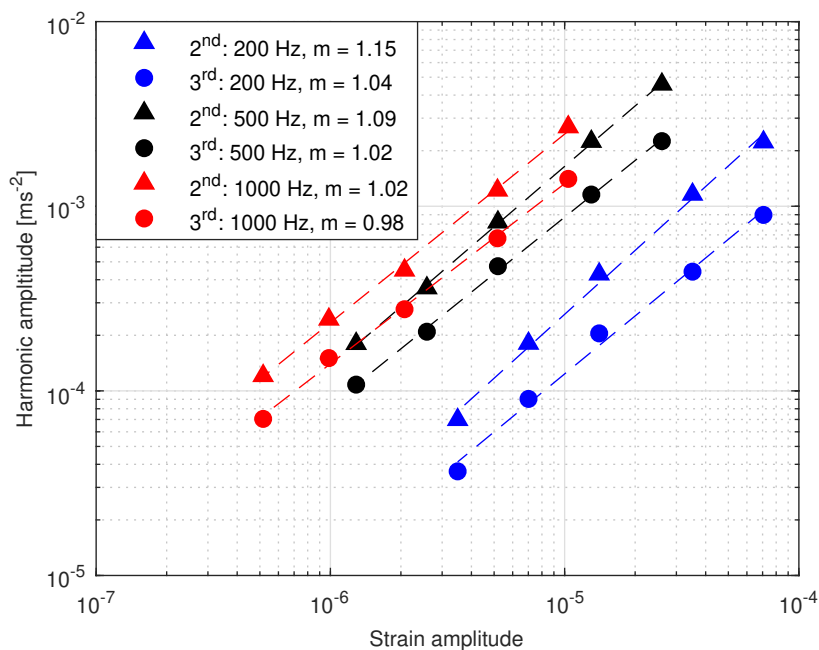
Figure 6-15: Second and third harmonics of the dynamic simulation with gaps activated.

Resonance shift

In Section 4-5, a frequency sweep was applied to the gravel at multiple excitation forces. Simulations of the same conditions were performed. As the FE model is restricted to motion only in one axis, only longitudinal modes can be excited. A wide sweep is first used to locate the resonance peak which corresponds to the first longitudinal mode. For the first approach, this was found to be at roughly 280 Hz whereas the resonance peak of the gravel is at roughly 240 Hz. For the simulations, a narrower sweep was applied to reduce computational time. The sweep was applied from 100 - 400 Hz over 1 s at amplitudes of 1, 5 and 100 N. The transfer function was calculated between the displacement and the input force at each amplitude (Fig. 6-16a). Unfortunately, this approach does not produce a resonance peak frequency shift. The peak stays fixed at 283.8 Hz which is in the range of the resonance peak of the gravel. Nevertheless, the resonance peak does decrease in amplitude as the driving force increases which is the same trend as the experimental data due to increasing losses.

When the gaps are enabled, a frequency shift can be produced (Fig. 6-16b). The peak frequency is produced at approximately 620 Hz which is over double that of the gravel's resonance peak at approximately 240 Hz. The peak resonance shifts to lower frequencies and the peak amplitude is decreased with increasing driving force, which is the same trend experienced by the experimental results. The resonance peak may be more accurately modelled with optimum model parameters.

(a) Without gaps. **(b)** With gaps.
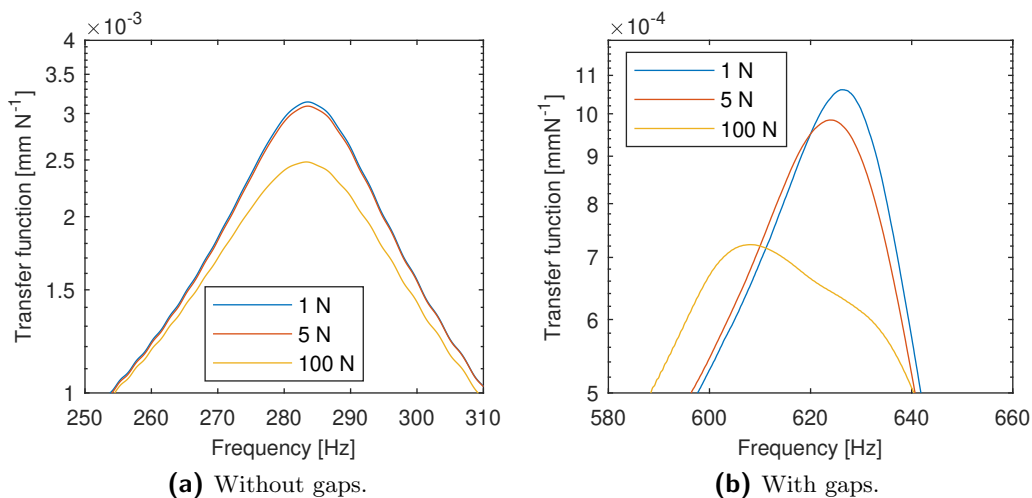
Figure 6-16: Resonance frequency shift of the dynamic simulation (a) with and (b) without gap functionality.

6-4-3 Discussion

The quasi-static and dynamic models recognise very different parameters. The comparison of the spring constants and yield forces between the two cases are shown in Figure 6-17. The spring constant of the yielding springs is larger than the non-yielding springs for both cases. The spring constants across all elements are greater for the quasi-static case than the dynamic case. The yield forces are much higher in the static model than the dynamic model as the

forces used in the quasi-static tests are much larger. This all points to a multi-scale effect where both the quasi-static model parameters and dynamic model parameters can coexist without effecting one another. Consider combining 50 COMBIN40 elements defined by the quasi-static model parameters with 50 COMBIN40 elements defined by the dynamic model parameters, to create a model with a total of 100 elements. At the low forces experienced in the dynamic case, the displacement experienced is much smaller than the gaps defined in the 50 quasi-static elements, therefore no gaps close and no force is experienced in these elements. At high forces experienced in the quasi-static case, the dynamic elements contain springs that yield at negligibly small forces compared to the total force. In addition, the non-yielding springs are much weaker than the springs in the quasi-static case, therefore the force from the dynamic springs is negligible compared to the total force.

(a) Spring constants.   **(b)** Yield forces.
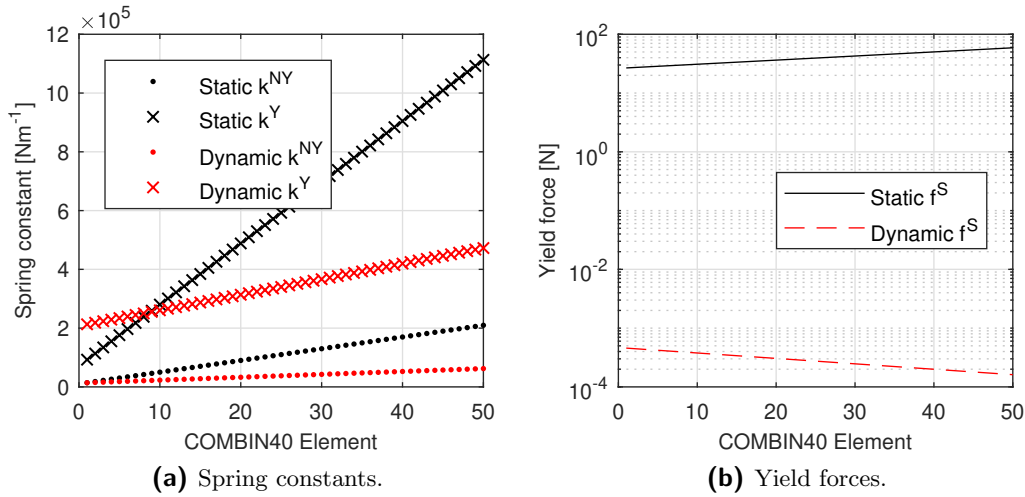
Figure 6-17: Comparison of model parameters between quasi-static and dynamic model.

The results from activating gap functionality in the elements cannot be directly compared to the experimental data as the model parameters have not been optimised. However, the parametric tests can be used to investigate the differences between the first approach, where gaps are absent, and the second approach, with gaps. Although, a suitable fit between the first approach and experimental stress-loops has been made, they do not produce both odd and even harmonics or produce a resonance shift, which are both key indicators of nonlinearity. The second approach produces both odd and even harmonics and a resonance shift is recreated. These are key indicators of nonlinearity and there absence makes utilising the gaps a strategy to progress.

The FE model produced here shows both classical and hysteretic nonlinear properties which replicates the true response of unconsolidated granulates. The PM approach (Preisach, 1935; Mayergoyz, 1985) and the method of modelling the Hertzian stick-slip motion by Aleshin and Van Den Abeele (2012) are purely hysteretic models, thus are not advantageous in this regard. Furthermore, the modelling technique used here allows a true FEM model to be made based on discrete elements which is not possible for the mathematical approaches. Therefore, it makes this spring-slider approach a much more viable option for modelling granular media from experimental data where further effects on the gravel can be investigated efficiently.

Chapter 7

Conclusions and outlook

7-1 Summary and conclusions

In this thesis, analysis of structural waves and vibrations was used to investigate the elastic behaviour of unconsolidated granulates. In the first stage, the nonlinear elastic properties were inquired experimentally with quasi-static and dynamic excitation forces. The analysis of the acquired data focussed on quantitatively describing the nonlinearity of granular media. Three types of materials were tested. Firstly, small scale ballast was used, a gravel, which retains the highly angular and rocky nature of ballast. Two sizes of uniform steel spheres, 5 and 10 mm diameter, were also tested to provide information on bulk material properties and particle size. A versatile experimental set-up to measure the amplitude-dependent stiffness was conceived. This allows the macroscopic effects of the nonlinear material to be addressed, such as harmonic wave distortion, resonance peak shift and the generation of higher harmonics. In addition, the propagation of structural waves through granulates was investigated, focussing on the role damping plays. This analysis assesses different thicknesses of granular material, the effect of different particle sizes on the transfer function and quantifying how damping is related to transmission losses. The elastic behaviour of the gravel and steel spheres shows a strong coherence to the same tests carried on on granular media in previous works. The main findings of the experimental data are:

- Quasi-static stress cycles of the gravel produce hysteretic loops. The loops highlight the highly nonlinear behaviour of the material and also reveal strain softening and plastic compaction properties.

- The gravel has a Young's modulus of 63.5 MPa which is quantitatively extracted from the shift in the peak resonance frequency. Both sizes of steel spheres have a Young's modulus approximately double the value for gravel. This is 3 orders of magnitude lower than the Young's modulus for steel, indicating that the bulk material stiffness has been homogenised. The resonance peak shifts to lower frequencies with increasing driving force.

- The gravel produces even and odd harmonics when excited with a monofrequency source. The odd harmonics have a greater amplitude than the even harmonics revealing there is a component of classical nonlinearity present. Analysis of the 2nd and 3rd harmonics reveals a linear relationship between harmonic and strain amplitudes for all three materials. The slope of the curves differs between the materials: a slope of approximately 1 is produced by the gravel whereas the steel spheres both produce a slope of approximately 2. This is related to the nonlinear coefficients that define the stress-strain relation.

- The transmission of waves through the gravel is significantly reduced at frequencies above a cut-off of 1000 Hz. Increasing the thickness of the gravel does not affect the cut-off frequency, however it does increase the transmission losses at frequencies above this. This implies that noise and vibrational disturbance above the cut-off frequency will be highly damped from a thick ballast bed.

In a second phase, the experimental data were used to create a model of the gravel. As the gravel is highly nonlinear, simulating its behaviour is not a straightforward task. Firstly, as nonlinear materials are frequency-dependent they cannot be simulated in the frequency domain and transient analyses must be performed instead. This makes nonlinear analyses time consuming especially as multiple simulations must be run at different input amplitudes due to the amplitude dependence of nonlinear materials. There are no standard nonlinear models that describe the behaviour of granular media. Many elasto-plastic models do exist, but they do not show features such as strain softening and hysteresis that granular media exhibit. If models of the railway superstructure are to capture an accurate structural response, the nonlinear behaviour of the ballast must be captured. FEM is used to model the railway superstructure as it allows multiple components with varying material properties to be modelled and handles complex geometries well. Typically, material models are entered as homogenised material properties and the entire structural network has to be discretised. However, the FEM approach used to model granular media in this thesis is completely new. A set of spring-slider elements are used as opposed to implementing a homogenised material model. Each element was parameterised by two spring constants, a yield force and an initial gap. Defining a distribution of these parameters allows for the creation of arbitrary hysteresis loops. Suitable model parameters were found using a genetic algorithm using an analytical model of 50 elements. The results of the parameter fitting were recreated in the FE model. This has huge benefits as only 50 nonlinear elements are simulated instead of thousands of elements in traditional material models where the entire structural volume is discretised. This allows simulations to be run faster and allows more effects to be investigated efficiently. The produced FE model was used to simulate the quasi-static and dynamic cases where the experimental conditions are replicated. The main findings from the FE model are:

- A set of parameters are optimised for the quasi-static model using an analytical model of static behaviour. The FE simulation is quite effective in capturing the experimental stress cycles and especially the plastic deformation observed. The simulated results have a very good fit to the unloading slopes but there is room for improvement in the loading curves.

- A different set of model parameters is optimised for the dynamic case but with gap functionality of the elements disabled, due to the difficulty of implementing gaps in an

analytical model. A multi-scale effect is noted where the two sets of parameters could coexist in the same model without affecting one another, but this is not tested. The model parameters provide a good fit for the dynamic stress loops, but increasing the input amplitude results in increasing misfit between the simulated and experimental dynamic loops.

- The model parameters for the FE model with gaps are not optimised for the experimental data, so simulations do not replicate the dynamic stress loops accurately. A parametric investigation of gap functionality must be done instead. Gap functionality allows asymmetric stress-loops to be created which are present in the experimental data at excitation frequencies below 200 Hz. In addition, figure-8 shaped loops can be reproduced at low amplitudes which are present in the experimental data at an excitation frequency of 100 Hz.

- Optimised model parameters for the dynamic simulations without gap functionality do not produce odd harmonics or exhibit an amplitude-dependent resonance frequency shift, as experienced by the experimental data. When gap functionality is introduced to 40 of the FE elements, both odd and even harmonics are produced and a resonance shift can be simulated. Analysis of the second and third harmonic reveals a linear relationship between the harmonic and strain amplitude. The slope is approximately 1 which matches the experimental data. The resonance frequency shifts to lower frequencies with increasing input amplitude as experienced by the experimental data but the resonance peak appears at twice the frequency experienced by the gravel.

- To find the best fit for different driving frequencies, the damping coefficient needs to be altered. This indicates frequency-dependent damping is required but this is not quantified. Damping exists both from inherent material damping and hysteretic damping, the damping coefficient only represents the material damping.

7-2   Outlook

7-2-1   Experimental studies

An important point that needs to be raised is that the experimental results have been established from gravel and not true railway ballast. Due to nonlinearity, the parameters cannot simply be scaled between the two particle sizes. However, the conclusions show that it is possible to extract information from this type of material and therefore there is little reason to doubt that the same experiments on true railway ballast would yield invaluable results. Therefore, data has to be acquired using true railway ballast whether it be from laboratory experiments or from a track-side field campaign. Track-side dynamic tests of the sleepers on the ballast would provide better transmission results where the sleeper has been properly embedded in the ballast.

7-2-2   Finite element model

The FE model produced here is the first step to achieve a fully functioning spring-slider model that represents nonlinear behaviour well in a variety of situations. Based on the conclusions

of the Finite Element model, it is possible to recreate some if not all of the quasi-static and dynamic behaviour of unconsolidated granular material using a model comprised of spring-slider elements, proving the concept. Much more work remains to be done to understand the effects of the parameter distribution and the interplay between the sliders and gaps. Presented below are a selection of promising suggestions to progress the validity of the FE model:

- Classical nonlinear springs should be introduced into the model as it may produce a better fit of the quasi-static stress cycles during loading. Currently, the latter part of the loading curves are linear whereas they exhibit curvature in the experimental data.

- The multi-scale effect mentioned in the discussion of FE model should be investigated. This would be done by combining the model for the quasi-static case and the model for the dynamic case in parallel, and repeating the simulations carried out here to see if the results are the same. In addition, running simulations at forces intermediate to those experienced by the quasi-static and dynamic tests to investigate to effect of forces outside of the two cases.

- Extra degrees of freedom to the movement of the spring-slider elements should be added to represent the motion in all three axial directions. Currently, the elements are only free to move in one direction, so only the longitudinal modes are captured. The extra degrees of freedom would allow bending modes to occur which would better represent the true response of the material.

- For the dynamic simulations, a quantitative study of frequency-dependent damping should be carried out. This is important as the damping varies between different driving frequencies.

- The positioning of the elements can be investigated, as currently all elements are attached to the block at the same point. The spring position may be generated randomly or an ordered arrangement used. The block can be substituted for an elastic structure as currently it is rigid.

- There is the possibility to expand the scope of the model to investigate other unconsolidated granulates such as rocks and soils. It may also be possible to model nonlinear features such as cracks and buckling.

Bibliography

Aleshin, V. and Van Den Abeele, K. (2012). Hertz–mindlin problem for arbitrary oblique 2d loading: General solution by memory diagrams. *Journal of the Mechanics and Physics of Solids*, 60(1):14–36.

Boitnott, G. (1993). Fundamental observations concerning hysteresis in the deformation of intact and jointed rock with applications to nonlinear attenuation in the near source region. In *Proceedings of the Numerical Modeling for Underground Nuclear Test Monitoring Symposium, Los Alamos Natl. Lab. Rev., LA-UR-93*, volume 3839, page 121.

Gist, G. A. (1994). Fluid effects on velocity and attenuation in sandstones. *The Journal of the Acoustical Society of America*, 96(2):1158–1173.

Guyer, R., McCall, K., Boitnott, G., Hilbert Jr, L., and Plona, T. (1997). Quantitative implementation of preisach-mayergoyz space to find static and dynamic elastic moduli in rock. *Journal of Geophysical Research: Solid Earth*, 102(B3):5281–5293.

Guyer, R. A. and Johnson, P. A. (2009). *Nonlinear mesoscopic elasticity: the complex behaviour of rocks, soil, concrete*. John Wiley & Sons.

Holcomb, D. J. (1981). Memory, relaxation, and microfracturing in dilatant rock. *Journal of Geophysical Research: Solid Earth*, 86(B7):6235–6248.

Indraratna, B., Ionescu, D., Christie, D., and Chowdhury, R. (1997). Compression and degradation of railway ballast under one-dimensional consolidation. *Australian Geomechanics Journal*, pages 48–61.

Indraratna, B., Thakur, P. K., and Vinod, J. S. (2009). Experimental and numerical study of railway ballast behavior under cyclic loading. *International Journal of Geomechanics*, 10(4):136–144.

Inserra, C., Tournat, V., and Gusev, V. (2008). Characterization of granular compaction by nonlinear acoustic resonance method. *Applied physics letters*, 92(19):191916.

Iwan, W. D. (1966). A distributed-element model for hysteresis and its steady-state dynamic response. *Journal of Applied Mechanics*, 33(4):893–900.

Johnson, P. and Rasolofosaon, P. (1996). Manifestation of nonlinear elasticity in rock: convincing evidence over large frequency and strain intervals from laboratory studies. *Nonlinear processes in geophysics*, 3(2):77–88.

Johnson, P. A. and Jia, X. (2005). Nonlinear dynamics, granular media and dynamic earthquake triggering. *Nature*, 437(7060):871.

Johnson, P. A., Zinszner, B., and Rasolofosaon, P. N. J. (1996). Resonance and elastic nonlinear phenomena in rock. *Journal of Geophysical Research: Solid Earth*, 101(B5):11553–11564.

Knight, J. B., Fandrich, C. G., Lau, C. N., Jaeger, H. M., and Nagel, S. R. (1995). Density relaxation in a vibrated granular material. *Phys. Rev. E*, 51:3957–3963.

Mavko, G., Mukerji, T., and Dvorkin, J. (2009). *The rock physics handbook: Tools for seismic analysis of porous media*. Cambridge university press.

Mayergoyz, I. (1985). Hysteresis models from the mathematical and control theory points of view. *Journal of Applied Physics*, 57(8):3803–3805.

McCall, K. (1994). Theoretical study of nonlinear elastic wave propagation. *Journal of Geophysical Research: Solid Earth*, 99(B2):2591–2600.

Mundrey, J. (2009). *Railway track engineering*. Tata McGraw-Hill Education.

Nazarov, V. E., Ostrovsky, L. A., Soustova, I. A., and Sutin, A. M. (1988). Nonlinear acoustics of micro-inhomogeneous media. *Physics of the Earth and Planetary Interiors*, 50(1):65 – 73.

Ostrovsky, L. and Johnson, P. (2001). Dynamic nonlinear elasticity in geomaterials. *Rivista del nuovo cimento*, 24(7):1–46.

Preisach, F. (1935). Über die magnetische nachwirkung. *Zeitschrift für physik*, 94(5-6):277–302.

Remillieux, M. C., Ulrich, T. J., Goodman, H. E., and Cate, J. A. T. (2017). Propagation of a finiteamplitude elastic pulse in a bar of berea sandstone: A detailed look at the mechanisms of classical nonlinearity, hysteresis, and nonequilibrium dynamics. *Journal of Geophysical Research: Solid Earth*, 122(11):8892–8909.

Richard, P., Nicodemi, M., Delannay, R., Ribiere, P., and Bideau, D. (2005). Slow relaxation and compaction of granular systems. *Nature materials*, 4(2):121.

Sayeed, M. A. and Shahin, M. A. (2016). Three-dimensional numerical modelling of ballasted railway track foundations for high-speed trains with special reference to critical speed. *Transportation Geotechnics*, 6:55–65.

Selig, E. T. and Waters, J. M. (1994). *Track geotechnology and substructure management*. Thomas Telford.

TenCate, J. A. and Shankland, T. J. (1996). Slow dynamics in the nonlinear elastic response of berea sandstone. *Geophysical Research Letters*, 23(21):3019–3022.

Tournat, V. and Gusev, V. (2010). Acoustics of unconsolidated model granular media: An overview of recent results and several open problems. *Acta Acustica united with Acustica*, 96(2):208–224.

Tournat, V. and Gusev, V. E. (2009). Nonlinear effects for coda-type elastic waves in stressed granular media. *Phys. Rev. E*, 80:011306.

Van Den Abeele, K. E., Johnson, P. A., Guyer, R. A., and McCall, K. R. (1997). On the quasi-analytic treatment of hysteretic nonlinear response in elastic wave propagation. *The Journal of the Acoustical Society of America*, 101(4):1885–1898.

Zhai, W., Wang, K., and H. Lin, J. (2004). Modeling and experiment of railway ballast vibrations. *Journal of Sound and Vibration*, 270:673–683.
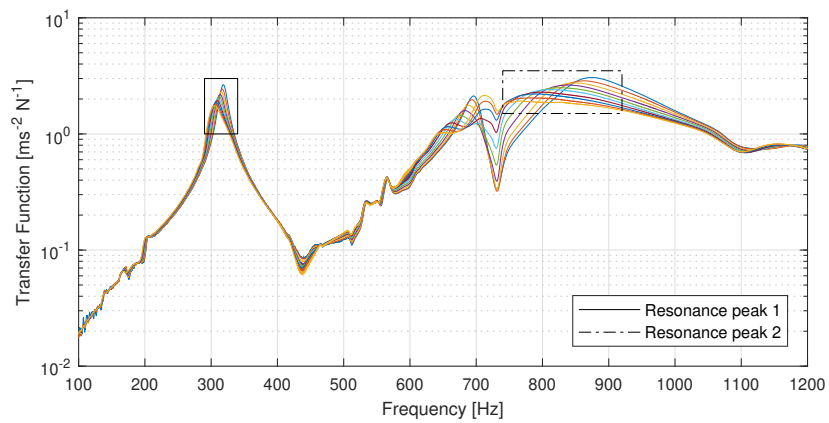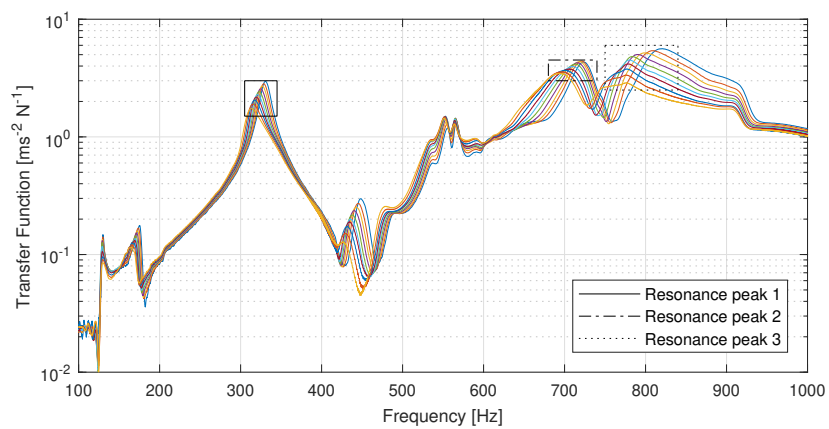
Appendix

(a)

(b)

Figure A-1: Transfer function for 5 mm diameter (a) and 10 mm diameter (b) steel spheres.

ETH

Eidgenössische Technische Hochschule Zürich
Swiss Federal Institute of Technology Zurich

Declaration of originality

The signed declaration of originality is a component of every semester paper, Bachelor's thesis, Master's thesis and any other degree paper undertaken during the course of studies, including the respective electronic versions.

Lecturers may also require a declaration of originality for other written papers compiled for their courses.

I hereby confirm that I am the sole author of the written work here enclosed and that I have compiled it in my own words. Parts excepted are corrections of form and content by the supervisor.

Title of work (in block letters):

STRUCTURAL WAVE PROPAGATION IN UNCONSOLIDATED GRANULATES

Authored by (in block letters):
For papers written by groups the names of all authors are required.

Name(s):	First name(s):
EVANS	LOUIS JAMES

With my signature I confirm that
- I have committed none of the forms of plagiarism described in the 'Citation etiquette' information sheet.
- I have documented all methods, data and processes truthfully.
- I have not manipulated any data.
- I have mentioned all persons who were significant facilitators of the work.

I am aware that the work may be screened electronically for plagiarism.

Place, date	Signature(s)
DÜBENDORF, 10-AUG-18	*(signature)*

For papers written by groups the names of all authors are required. Their signatures collectively guarantee the entire content of the written paper.